International Journal of Solids and Structures 257 (2022) 111129

Contents lists available at ScienceDirect

International Journal of Solids and Structures

journal homepage: www.elsevier.com/locate/ijsolstr

Rate dependent fracture along a silicon/epoxy interface under mixed-mode loading conditions

Tianhao Yang [a], Vatsa Gandhi [b], Rui Huang [a], Kenneth M. Liechti [a,*]

[a] Center for the Mechanics of Solids, Structures and Materials, Department of Aerospace Engineering and Engineering Mechanics, University of Texas, Austin, TX 78712, USA
[b] GALCIT, California Institute of Technology, Pasadena, CA 91125, USA

ARTICLE INFO

Article history:
Received 8 February 2021
Received in revised form 3 June 2021
Accepted 8 June 2021
Available online 10 June 2021

Keywords:
Dual-actuator loading device
Laminated beam specimens
Mixed-mode fracture
Mixed-mode foundation analysis
Rate dependent fracture

ABSTRACT

This paper describes the development of a dual-actuator loading device that was then used to apply asymmetric, transverse end-displacements to laminated beam specimens (silicon/epoxy/silicon) over a range of separation rates. Measurements of the reaction forces, as well as load-point displacements and rotations, were used to determine the normal and tangential components of the crack tip displacements and the corresponding components of the J-integral. This was made possible because the specimens identically satisfied a balance condition. The resulting data set obtained from experiments conducted at five separation rates at each of five mode-mix phase angles is a testimony to the efficiency of the approach. A mixed-mode beam on elastic foundation analysis established that the stiffness of the normal and shear interactions of the silicon/epoxy interface was independent of the separation rate and mode-mix. Furthermore, the stiffness values thus determined were considerably lower than those based on the bulk behavior of the epoxy in tension and shear. The analysis also allowed the crack growth to be tracked in order to establish its onset and the corresponding critical values of the normal and shear components of the J-integral, along with the corresponding strengths and critical crack tip displacements. For each mode-mix, these critical values increased with the separation rate. This increase in properties is in spite of the glassy nature of the bulk epoxy and further suggests the presence of an interphase region in the epoxy adjacent to the silicon. However, the change of mode-mix was accompanied by a change in local separation rates, leading to non-monotonic behavior in the critical J-integral. Following the onset of crack growth, the application of the transverse end-displacements along radial loading paths resulted in simultaneous changes in the local separation rates and mode-mix, implying a fracture criterion that depends on both mode-mix and rate-dependent damage evolution processes.

1. Introduction

Interfaces abound in many technologically important applications that range from primary structural adhesively bonded joints in aerospace, naval and automotive structures to the multiple interfaces that are common in microelectronics devices and packaging. One potential failure mode in all these heterogeneous systems is interfacial delamination, which can be addressed via fracture mechanics analyses quantifying the strength and durability for design purposes.

Delamination analyses based on interfacial fracture mechanics concepts were pioneered by Williams (1959) and effectively put into practice by Rice (1988) and Hutchinson and Suo (1992). A striking feature of interfacial fracture mechanics is that the toughness is often a function of the relative amount of tensile and shear tractions on the interface (Chai and Liechti, 1992; Evans et al., 1990; Wang and Suo, 1990) when the crack is constrained to grow along an interface. The toughening of interfaces with increasing shear component has generally been attributed to asperity locking (Evans and Hutchinson, 1989) or increased plastic or viscoplastic dissipation (Chai and Liechti, 1992; Swadener and Liechti, 1998) near the crack front. This so-called linearly elastic fracture mechanics (LEFM) approach is generally sufficient in accounting for the behavior of preexisting flaws as long as the fracture process zone is sufficiently small (Parmigiani and Thouless, 2007; Sills and Thouless, 2013). Alternatively, cohesive zone modeling can accommodate delamination with larger fracture process zones and without the requirement of a preexisting flaw (Mohammed and Liechti, 2000). The ideas behind cohesive zone modeling were originally proposed by Dugdale (1960) and Barenblatt (1959) in order to mitigate the stress singularities that

* Corresponding author.
E-mail address: kml@mail.utexas.edu (K.M. Liechti).

https://doi.org/10.1016/j.ijsolstr.2021.111129
0020-7683/

are the hallmark of LEFM. Since then, it has been applied to interfacial crack growth problems in general (Needleman, 1990), delamination in adhesively bonded joints (Högberg et al., 2007; Liand Thouless, 2006; Sorensen, 2002; Ungsuwarungsri and Knauss, 1987), laminated, fiber-reinforced composite materials (Blackman et al., 2003) and thin films (Shirani and Liechti, 1998) as well as adhesive contact problems (Johnson et al. (1971); Maugis (1992)), as some early examples in an extensive array of literature.

Cohesive zone modeling typically requires a traction-separation relation as the constitutive representation of the interactions between the surfaces. The traction-separation relation for a specific interaction can be determined experimentally by direct or indirect methods (Gowrishankar et al., 2012). The direct method requires two components: the path-independent J-integral and the crack tip displacement, which can be challenging for experiments and may suffer from resolution issues. For materials that are transparent to visible or infrared radiation, crack opening interferometry has been used to characterize the crack tip behavior (Gowrishankar et al., 2012; Mello and Liechti, 2006; Wu et al., 2016). The method can have a resolution of 20 nm and the full crack front can be observed. However, only normal crack tip displacements can be measured.

Several approaches based on digital image correlation (DIC) have been introduced recently. Blaysat et al. (2015) developed a parameter identification approach based on the kinematics of double cantilever beam specimens and concepts from integrated DIC, where the unknown degrees of freedom are the properties that define a traction-separation relation, rather than displacements and rotations, thereby increasing computational efficiency and robustness. Gorman and Thouless (2019) conducted an extensive study of the use of DIC for tracking the evolution of the cohesive zone and extracting traction-separation relations. In a study of the rate dependence of fracture between polymer modified bitumen and aluminum under mode I loading (Rajan et al., 2018), two stereo DIC systems were used. One, operating at higher magnification, was focused on the crack tip region to measure the crack tip opening displacement with a resolution of approximately 40 nm. The low magnification system was used to determine the strains ahead of the crack tip as well as the load line displacement. The same group has recently extracted the mode I and mode II traction-separation relations of uncured thermoset tows using a rigid double cantilever beam arrangement in combination with DIC (Rajan et al., 2020).

In the current paper, we investigate the effects of rate and mode-mix on fracture of an interface by following the direct method (Ouyang and Li, 2009; Wu et al., 2019), which significantly simplified the J-integral concept for mixed-mode fracture and allowed the crack tip displacements to be determined from the remote measurements at the loading point. The cohesive traction at the interface is then attained as the derivative of the J-integral with respect to the local separation (Sorensen and Jacobsen (2003)), under the assumption that the same traction-separation relations are followed along the interface. Wu et al. (2019) utilized the reflection of a laser beam on a 45° mirror to measure the end rotations of end-loaded split (ELS) and end-notched flexure (ENF) specimens, which offered a resolution of $\sim 10^{-4}$ rad. However, the range of the beam deflection was restricted by the size of the position sensing detector, which was used to receive the reflection beam signal. Here, we have found that DIC is simpler and more robust in measuring the end displacements and rotations. It provides the trajectory of the beam deflection all the way to the crack tip in order to determine the normal and tangential components of the J-integral and crack tip displacements. It also allows the mode-mix to be controlled more easily than using a selection of asymmetric specimens.

Many test methods have been successfully developed for characterizing fracture at interfaces under all three fracture modes and combinations thereof. The most commonly used type of specimen for determining the fracture toughness of a bi-material system is the double cantilever beam specimen as established by Kanninen (1973). As a logical evolution from quasi-static testing with double cantilever beam specimens, alternative specimen geometries, such as reinforced adherends (Jain et al., 1998; Marzi et al., 2014) and tapered adherends (Brussat et al., 1977), were studied for measuring the mode I fracture toughness at high separation rates. Mixed-mode interactions have been characterized by introducing asymmetries either in the specimen geometry and materials or loading conditions. Examples of mixed-mode fracture tests with asymmetry in the specimen geometry and materials include the asymmetric double cantilever beam (Sundararaman and Davidson, 1997; Xiao et al., 1993), four-point flexure and composite cylinder (Cao and Evans, 1989; Charalambides et al., 1990), the end loaded split (Hutchinson and Suo, 1992; Wang and Vu-Khanh, 1996), and the compact tension shear specimens (Mahajan and Ravi-Chandar, 1989). Most of these previous works focused on the effect of mode-mix on the fracture toughness following the LEFM approach. It remains a challenge to characterize the mixed-mode traction-separation relations for an interface (Sorensen and Jacobsen, 2003). A direct method was proposed by Wu et al. (2016) to determine mixed-mode traction–separation relations based on a combination of global and local measurements using the end loaded split (ELS) configuration for a silicon-epoxy interface, where the epoxy thickness was varied to obtain phase angles ranging from −42° to 0°. More recently, mixed-mode traction-separation relations were extracted directly for a silicon/epoxy interface with phase angles ranging from −53° to 87.5°, using asymmetrical end-notch flexure and end-loaded split specimens with different adherend materials (Wu et al., 2019).

Asymmetry can also be introduced by applying uneven loads to a symmetric laminate. Reeder and Crews (1990) pursued such an approach to study mixed-mode fracture in laminated fiber reinforced composites. Similarly, Fernlund and Spelt (1994) developed a complex loading jig consisting of a linkage system which induced an asymmetry in the forces acting on the upper and lower adherends. Davidson and Sediles (2011) went a step further by developing a device that made use of bending and torsion on a laminate to produce all three fracture modes. Although none of these devices were used to extract traction-separation relations, there were some questions from a theoretical standpoint (Suo et al., 1992) as to the suitability of applying uneven end loads rather than moments for providing fracture properties under large scale bridging conditions. Because configurations that employ uneven end moments (Jacobsen and Sørensen, 2001; Lindhagen and Berglund, 2000; Sørensen and Jacobsen, 2009, 1998) provide crack tip stress fields that are invariant with crack length, it was postulated that they would provide true material properties, uninfluenced by structural effects. This point has recently been addressed by Pappas and Botsis (2019), who also developed a more convenient way to apply uneven bending moments. They found that applying uneven end loads or moments to an adhesively bonded laminate resulted in very similar traction-separation relations even though the damage zone was relatively large. On the other hand, the same was not true of a laminated fiber reinforced polymer with a large and complex bridging zone.

All the approaches for controlling mode-mix that have been discussed so far are inherently proportional loading devices, which do not allow the effects of more complex mixed-mode loading paths to be followed. Biaxial loading devices (Chai and Liechti, 1991; Liechti and Knauss, 1982; Mello and Liechti, 2004) that apply uniform tension and shear to a bimaterial strip are certainly capable of achieving such a goal, but are complex. A conceptually simpler

approach was provided by Singh et al. (2010) who used a dual actuator device to apply uneven end loads to a symmetric laminate. The approach taken here mirrors their approach, albeit with simpler actuation due to the relatively low loads that were required here. The device has recently been used to study the rate-dependent fracture of a silicon/epoxy interface under the nominally mode-I condition with symmetric loading (Yang et al., 2020).

The remainder of this paper is organized as follows. In section 2, we describe the configurations of the experimental setup and the specimen preparations in detail. Then we present a series of analyses in section 3 concerning the design of the experiments, the mode-mix analysis, and the post processing of the raw data for extraction of the mixed-mode properties. Next, a complete set of results are displayed in section 4 where the effects of the separation rate and mode-mix are discussed at length. Conclusions are provided in section 5.

2. Experiments

The dual-actuator device (Fig. 1) consists of three parts: the support structure, the specimen mount, and the data acquisition system. The rods of the support structure (Fig. 1a) are secured to a table using a thick aluminum block while aluminum clamps are used to grip the actuators and the specimen. The vertical post on the right provides support for the clamped end of the specimen. Stress concentrations due to the clamp are mitigated by a layer of Teflon© tape, thereby reducing the possibility of breaking the clamped end of the specimen. Two U-shaped loading tabs are bonded to the top and bottom surfaces of the specimen where the end-displacements are applied. Rod ends are then used to link the loading tabs to the load cells and the actuators (Fig. 1b). They allow for rotation and any relative lateral movement of the loading tabs. Two DC motor actuators (PI M227.25), with a maximum extension capability of 25 mm and a maximum travel velocity of 0.75 mm/s, are controlled using the controller (PI Mercury C-863) that receives commands via LabVIEW VI from a computer. The actuators are independently controlled in order to provide the specified rates for both end-displacements. Their specifications are summarized in Table 1.

The measurement system consists of two load cells and a camera for DIC. The tension/compression load cells (Omega LCMFL-20 N) are threaded onto an adapter which resides on the tips of each actuator. These load cells are connected to their respective Wheatstone bridges and amplifiers so that the voltage output from the load cells can be acquired via a data acquisition board that is controlled by the same LabVIEW program. As the actuator extends or contracts, the beams of the specimen experience a loading condition that causes a delamination crack to propagate while the corresponding loads are registered using the load cells. DIC targets are attached to the two loading tabs in order to obtain the normal and tangential end-displacements as well as end-rotations (Fig. 1c). The motions of the targets are captured using a 2.2 megapixel CMOS camera (Lumenera LT225) with a maximum framerate of 170 frames per second. However, while an experiment is running, the maximum rate is limited to 50 frames per second by the input/output characteristics of the computer. A magnifying lens (TEC-55 Computar) is used for enhancing the precision of the DIC. Image acquisition is triggered in LabVIEW so that the actuator control and data acquisition are all synchronized. The DIC analysis is conducted on selected regions of the two targets using GOM Correlate Software to obtain the end displacements and rotations.

The fracture specimen (Fig. 2) consists of two silicon beams bonded by a layer of epoxy (EP30, Master Bond Inc.) using 50 × 5 mm silicon strips that were diced from silicon wafers. The mechanical behavior of the epoxy was characterized by conducting uniaxial tensile tests and Arcan shear tests (Hung and Liechti, 1997; Liang and Liechti, 1995) in a universal testing machine (Instron). The deformation of the epoxy was recorded by a camera and the local strain was obtained through DIC. The stress–strain curve in tension is shown in Supplementary Fig. S1. The Young's modulus of the epoxy was obtained from the unloading (or second loading) curve as 2.4 GPa. The tensile yield strength of the epoxy was estimated to be 36 MPa. No stress plateau was reached and the epoxy eventually failed at about 4.2% strain. The uniaxial tensile test was conducted at two other strain rates (Fig. S1b), showing that the epoxy behaved in a rather glassy man-

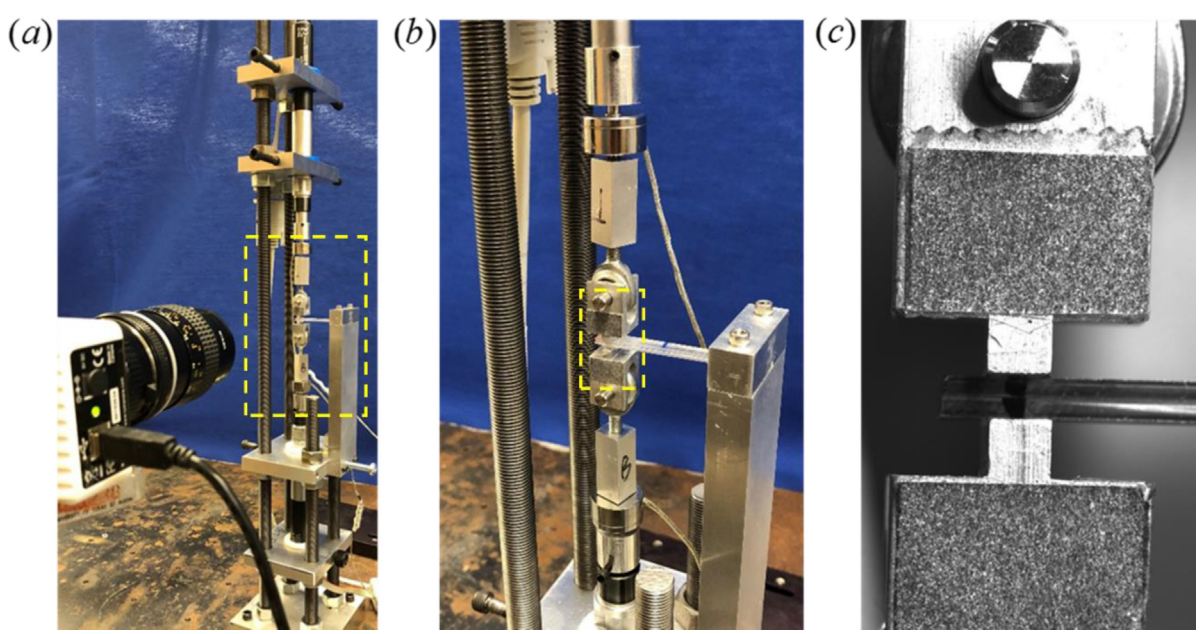

Fig. 1. (a) Dual-actuator loading device; (b) Specimen grips and installation (boxed region in a); (c) An image of the DIC target taken by the camera during the experiment (boxed region in b).

Table 1
Actuator specifications and property descriptions.

Property	Description	Specifications
Travel range	Maximum extension of an actuator	25 mm
Design resolution	Resolution for position values recorded by the controller	0.0035μ m
Minimum incremental motion	Minimum extension of an actuator	0.05μ m
Maximum velocity	Maximum travel velocity of an actuator	0.75 mm/s
Maximum force	Maximum force an actuator arm can withstand during extension or contraction	±40 N

ner at the relatively high strain rates ($\dot{\varepsilon} \geq 10^{-4}$/s). During the double cantilever beam experiment, the local strain rate turned out to be large enough ($\dot{\varepsilon}$ 10^{-2}/s) at the crack tip of the silicon/epoxy interface so that the epoxy was assumed to be in its glassy state and hence linearly elastic.

The Arcan shear tests were also conducted at three different strain rates. The corresponding stress–strain curves are shown in Fig. S2. The shear modulus increased with increasing shear rates, although the variation was relatively small so that the glassy shear modulus of the epoxy is taken to be 0.9 GPa at a shear strain rate of 10^{-2}/s. With the Young's modulus of 2.4 GPa from the uniaxial tensile test, the Poisson's ratio of the epoxy is taken to be 0.33. The 0.2% yield strength (~24 MPa) was the same for all three shear rates. The significance of the shear behavior of the epoxy is not seen in the mode I fracture experiments (Yang et al., 2020); however, it is essential in the mixed-mode experiments to check if any plasticity had been triggered in the epoxy layer by the relatively large shear stress at the silicon/epoxy interface. As it so happened for the present study, the maximum shear traction at the interface was less than 24 MPa and the maximum normal traction was less than 10 MPa, based on the stiffness values and the crack-tip displacements in Fig. 15.

The fracture specimens were prepared following the procedures specified in Yang et al. (2019), except that, in the current work, the initial crack length was fixed at ~12 mm from the loading point by coating a thin layer of Au/Pd film to the upper silicon beam. The thickness of the epoxy layer was controlled by a steel spacer with a thickness of 40 μm. The Au/Pd coating layer has a much smaller thickness of 15 nm, thereby providing a sharper crack front between the epoxy layer and the upper silicon beam. The benefit from specifying a common initial crack length across all specimens is to maintain a consistent relationship between the global separation rates at the loading point and the local rates at the crack tip, as will be discussed further in Section 4.2. Further details regarding the specimen geometry and the material properties are provided in Table 2.

3. Analysis

In this section, four sets of analysis are presented for the mixed-mode fracture experiment. First, an energy-based fracture criterion is adopted to determine the critical load levels and associated end displacements under mixed-mode loading conditions. This served to set design parameters for the selection of load cells and actuators as well as the resolution and range constraints on the DIC system. It is followed by an analysis of the nominal phase angle for the mixed-mode specimens. Then, a decoupled beam interaction analysis is employed to determine the normal and tangential components of the J-integral as well as the crack tip displacements. Finally, a mixed-mode beam on elastic foundation analysis is presented to enable extraction of the stiffness values of the normal and shear interactions as well as the critical J-integral and strength for crack extension from the remote measurements.

3.1. Critical load envelopes

For the purpose of selecting actuators and load cells with appropriate ranges of measurement, the force and the displacement that are required to achieve interfacial fracture along different loading paths (mode-mix) are estimated by a linearly elastic fracture mechanics (LEFM) approach based on a beam analysis. A common mixed-mode fracture criterion is adopted for the silicon/epoxy interface that is given by

$$\frac{G_I}{\Gamma_I} + \frac{G_{II}}{\Gamma_{II}} = 1 \tag{1}$$

where Γ_I and Γ_{II} are, respectively, the mode I and mode II fracture toughness of the interface, while G_I and G_{II} are the corresponding energy release rates ($0 \leqslant G_I \leqslant \Gamma_1$ and $0 \leqslant G_{II} \leqslant \Gamma_{II}$). In the parametric study that follows, critical loading envelopes were determined at various toughness ratios, $\Gamma_{II}/\Gamma_I = 1, 5, 10$, while the mode I tough-

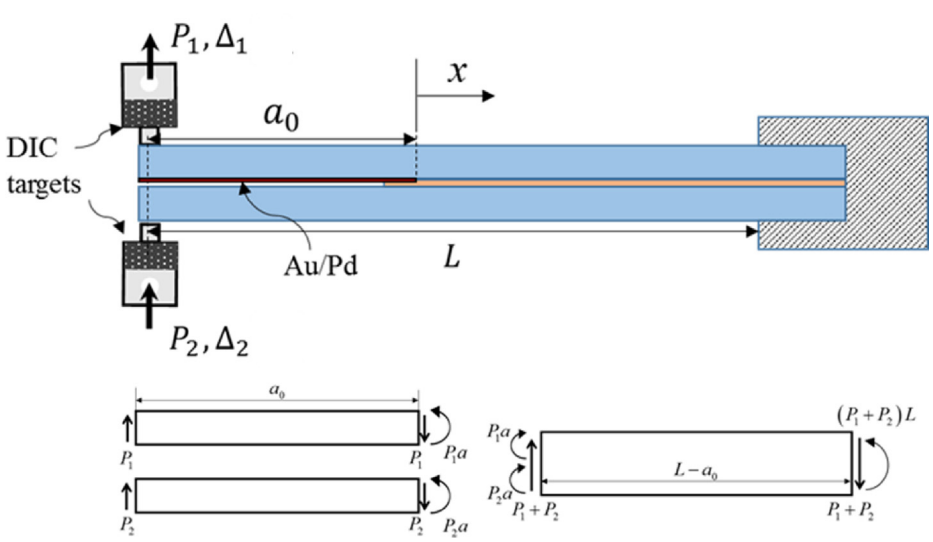

Fig. 2. Loading configuration of the laminated beam specimen and free-body diagrams (epoxy layer neglected).

Table 2
Relevant specimen geometry and materials properties.

Geometry					Materials			
Width b (mm)	Length L (mm)	Initial crack length a_0 (mm)	Silicon thickness h (mm)	Epoxy thickness h_e (mm)	Silicon Young's modulus E (GPa)	Silicon Poisson's ratio ν	Epoxy Young's modulus (GPa)	Epoxy Poisson's ratio
5.0	38.0	12.0	1.0	0.04	130	0.22	2.4	0.33

ness of the silicon/epoxy interface was taken to be 10 J/m^2 (Yang et al., 2019).

The specimen and loading configurations are depicted in Fig. 2. Direct far-field measurements include the applied forces (P_1, P_2), normal and tangential displacements $(\Delta_1, \Delta_2, U_1, U_2)$, and rotations (Θ_1, Θ_2), all at the loading ends of both the upper and lower beams. For design purposes, the system is simplified by neglecting the presence of the thin epoxy layer, and the corresponding free-body diagrams are given in Fig. 2. Following a simple beam analysis (Hutchinson and Suo, 1992), the energy release rate at the crack tip can be written in terms of the applied forces as

$$G = \frac{1}{2b}\left[\frac{(P_1 a_0)^2}{E_1 I_1} + \frac{(P_2 a_0)^2}{E_2 I_2} - \frac{(P_1 a_0 + P_2 a_0)^2}{qbE_2 h^3}\right] \tag{2}$$

where $E_1 = E_2 = \bar{E}$ and $I_1 = I_2 = \frac{bh^3}{12}$. Here, $\bar{E} = \frac{E}{1-\nu^2}$ denotes the plane-strain elastic modulus, and b, h refer to the width and thickness of the silicon beams, respectively. The quantity q is a measure of the elastic and geometry mismatch in the laminated beam system and its value is 2/3 for the symmetric double cantilever beam (DCB) specimen used in the present study.

The energy release rate in Eq. (2) can be further partitioned into mode I and mode II components based on (Williams, 1989) as $G = G_I + G_{II}$ and

$$G_I = \frac{3(P_1 - P_2)^2 a_0^2}{\bar{E} b^2 h^3} \tag{3}$$

$$G_{II} = \frac{9(P_1 + P_2)^2 a_0^2}{4\bar{E} b^2 h^3} \tag{4}$$

Note that, for this symmetric DCB specimen, Conroy et al. (2015) established that this partitioning approach is consistent with the one in (Hutchinson and Suo, 1992) based on the use of stress intensity factors. The phase angle of the fracture mode-mix based on the energy release rates is[1]

$$\Psi = \tan^{-1}\sqrt{\frac{G_{II}}{G_I}} \tag{5}$$

Combining Eqs. (1), (3) and (4), we obtain a critical load envelope (Fig. 3a) for each fracture toughness ratio (Γ_{II}/Γ_I), with each pair (P_1, P_2) being the critical values of the forces that trigger fracture at the interface based on the fracture criterion (Eq. (1)). Two special cases, $P_2 = -P_1$ $(P_1 > 0)$ and $P_2 = P_1$, correspond to pure mode I $(\Psi = 0)$ and mode II $(\Psi = \pm 90^\circ)$ conditions, respectively. The envelope is symmetric with respect to $P_1 + P_2 = 0$, but this only holds when the epoxy layer is ignored. The presence of the epoxy layer introduces an elastic mismatch and causes an unsymmetrical loading path, as discussed further in Section 3.2. When $\Gamma_2/\Gamma_1 = 10$, the range of the critical forces is bounded by 20 N. For sufficient measurement precision without exceeding the upper limit, we chose load cells with a 20 N capacity for the present study.

In order to establish a displacement envelope (Fig. 3b), we replace the force terms in Eqs. (3) and (4) with the applied displacements using the following relations,

$$P_1 = \frac{3E_1 I_1}{a_0^3(1+2\beta)}(\Delta_1 + \beta(\Delta_1 - \Delta_2)) \tag{6}$$

$$P_2 = \frac{3E_2 I_2}{a_0^3(1+2\beta)}(\Delta_2 - \beta(\Delta_1 - \Delta_2)) \tag{7}$$

where $\beta = \frac{1}{8}\left(\frac{L^3}{a_0^3} - 1\right)$. The above equations were derived from an elastic beam analysis under the assumption of perfect bonding (no separation) between the two beams except for the cracked portion ($x < 0$ in Fig. 2). The critical displacement under mode I fracture was estimated as 0.046 mm for both upper and lower beams. To ensure a reasonable amount of data (more than 20 data points) collected for each experiment and to accommodate data acquisition rates, the applied displacement rates were selected as 0.001, 0.005, 0.025, 0.125 and 0.625 mm/s. The displacement envelope also suggested that the applied displacement is bounded by 1.5 mm, which is 1/8 of the initial crack length (12 mm), thus justifying the use of the beam equations for analysis.

3.2. Nominal mode-mix

The dual-actuator loading device offers the flexibility to control the motion of the upper and lower beams independently. Therefore, a full range of mode-mix is feasible by varying the end displacement ratio (Δ_2/Δ_1). Combining equations (2)-(7), the nominal phase angle as a function of the applied displacement ratio is determined to be

$$\Psi = \tan^{-1}\left(\frac{2\sqrt{3}}{3 + (L/a)^3}\frac{1 + \Delta_2/\Delta_1}{1 - \Delta_2/\Delta_1}\right) \tag{8}$$

By Eq. (8), when $\Delta_2/\Delta_1 = -1$ $(\Delta_1 > 0)$, the specimen is subjected to symmetric opening displacements and pure mode I fracture is activated $(\Psi = 0^\circ)$. On the other hand, pure mode II $(\Psi = \pm 90^\circ)$ occurs when $\Delta_2/\Delta_1 = 1$. By varying the applied displacement ratio, we can obtain a full range of mode-mix (Fig. 4). With Eq. (8), we can also examine the effect of the crack length on the mode-mix when the presence of epoxy is ignored. As discussed in Appendix A, the mode-mix is not affected by the crack length for the two limiting cases with $\Delta_2/\Delta_1 = \pm 1$. However, for the mixed-mode cases, the phase angle increases as the crack grows (Fig. A1).

The presence of an epoxy layer leads to an elastic mismatch at the interface and a shift of the phase angle (Fig. 4) in the mode-mix compared to the corresponding homogeneous system (see Appendix A for more discussion). Nevertheless, the nominal phase angle from Eq. (8) is used here as a point of reference for discussion. With a view to exploring the full range of the mode-mix between pure mode-I $(\Psi = 0^\circ)$ and pure mode-II $(\Psi = 90^\circ)$, the mixed-mode experiments in this study were conducted at five displacement ratios $(J - integralsand\Delta_2/\Delta_1 = -1,\ 0.5,\ 0.7,\ 0.8$ and $0.95)$. For each displacement ratio, five specimens were loaded at five dis-

[1] The sign of the phase angle depends on the direction of the shear traction at the interface ahead of the crack tip, which cannot be determined from the energy release rates. However, in terms of the applied forces or displacements, the sign of the phase angle can be determined as in Eq. (8).

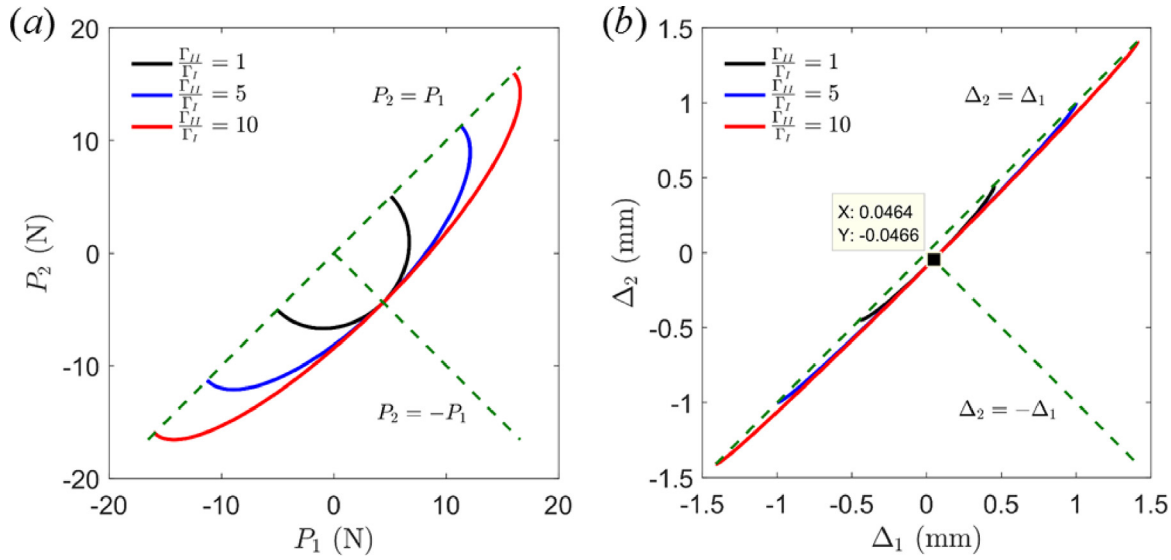

Fig. 3. (a) Critical load envelope and (b) displacement envelope for different ratios of fracture toughness ($\Gamma_1 = 10$ J/m^2), with $a_0/L = 0.32$.

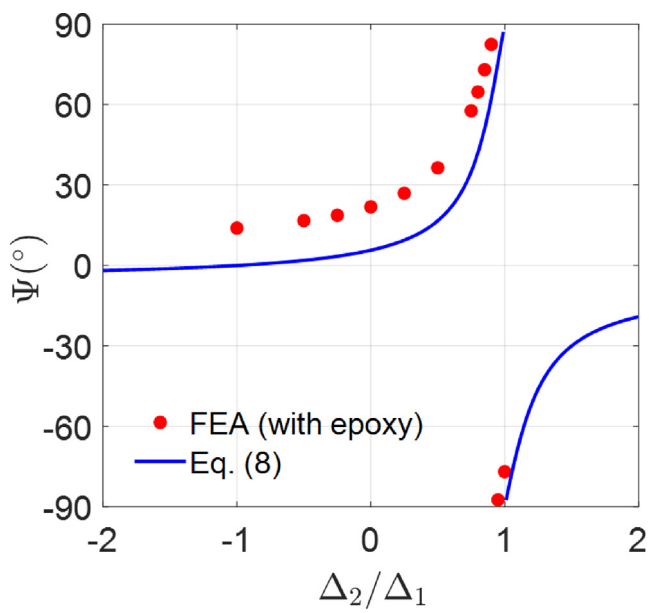

Fig. 4. Nominal phase angle of mode-mix as a function of the prescribed end displacement ratio for an initial crack length ($a_0/L = 0.32$), comparing Eq. (8) with those by a finite element model including the epoxy layer.

placement rates ($\dot{\Delta}_1$) ranging from 0.001 to 0.625 mm/s in order to study the rate effect.

3.3. J-integrals and crack tip displacements

Following the method proposed by (Wu et al., 2019), the normal and shear components of J-integral (J_1 and J_2) can be obtained for the symmetric double cantilever beam specimen as

$$J_1 = \frac{1}{2b}(P_1 - P_2)(\Theta_1 - \Theta_2) \tag{9}$$

$$J_2 = -\frac{3}{4bh}(P_1 + P_2)(U_1 - U_2) \tag{10}$$

We note that Eqs. (9–10) were derived from a linearly elastic beam analysis with the two silicon beams interacting via a traction-separation relation that is unknown *a priori* (Wu et al., 2019).[2] The presence of the epoxy layer is ignored in this analysis. It can be shown that the J-integral components in Eqs. (9–10) reduce to the mode-I and mode-II energy release rates in Eqs. (3–4) at the limiting case of LEFM when the interface is assumed to be fully bonded with no relative displacement ahead of the crack tip ($x \geq 0$ in Fig. 2). By Eqs. (9–10), the J-integrals can be determined directly from the remote measurements, without measuring the crack length.

Correspondingly, the components of the crack tip displacements can be obtained as (Wu et al., 2019):

$$\delta_n^* = (\Delta_1 - \Delta_2) - a(\Theta_1 - \Theta_2) + \frac{2a^3}{\bar{E}bh^3}(P_1 - P_2) \tag{11}$$

$$\delta_t^* = (U_1 - U_2) + \frac{3a^2}{\bar{E}bh^2}(P_1 + P_2) \tag{12}$$

Here, in addition to the remote measurements at the loading ends of the specimen, the crack length (a) is needed to determine the crack-tip displacements. In the present study, we measured the initial crack length (a_0) so that the normal and tangential displacements at the initial crack tip (δ_{n0}^* and δ_{t0}^*) can be readily determined. Once the crack starts growing, the crack length may be estimated by a beam on elastic foundation model (Gowrishankar et al. (2012)) and then the displacements at the new crack tip can also be estimated by Eqs. (11–12), with limited accuracy due to the assumption of a linear traction-separation relation.

Assuming that the interactions along the interface can be described by two traction-separation relations in the normal and tangential directions, each component of the J-integral equals the work done by the corresponding traction component at the initial crack tip. Consequently, the normal and shear tractions at the initial crack tip can be determined by

$$\sigma_{n0}^* = \frac{\partial J_1}{\partial \delta_{n0}^*} \tag{13}$$

[2] An approximation was used in Wu et al. (2019) for the tangential displacements at the loading end of the specimen, ($U_1 - U_2$), which is not needed in the present study because the lateral end-displacements were measured by DIC.

$$\sigma^*_{t0} = \frac{\partial J_2}{\partial \delta^*_{t0}} \tag{14}$$

which can be used for direct extraction of the traction-separation relations with the J-integrals and crack-tip displacements obtained by Eqs. (9–12) (Wu et al., 2019). However, if the traction-separation relations vary along the interface, due to the rate effects or the change in mode-mix, Eqs. (13–14) are no longer valid. Previously we have shown that the rate-dependent fracture led to different traction-separation relations within the cohesive zone under the mode-I condition (Yang et al., 2020, 2019). In the present study, under mixed-mode conditions, we show that the change of mode-mix during crack growth can also lead to different traction-separation relations along the interface in the same specimen.

3.4. A mixed-mode beam on elastic foundation analysis

A beam on elastic foundation model was presented previously (Gowrishankar et al. (2012)) for normal interactions only. Here, we extend the model to include both the normal and shear interactions at the interface (see details in Appendix B). For the normal interactions, we obtain

$$\tilde{P} = \frac{\bar{E}bh^3}{4a^3}\left(1 + \frac{3}{\lambda_n a} + \frac{3}{(\lambda_n a)^2} + \frac{3}{2(\lambda_n a)^3}\right)^{-1} \tilde{\Delta} \tag{15}$$

where $\tilde{P} = P_1 - P_2$, $\tilde{\Delta} = \Delta_1 - \Delta_2$, $\lambda_n = \left(\frac{6K_n}{\bar{E}h^3}\right)^{1/4}$, and K_n is the normal stiffness of the interface. Similarly, for the shear interactions, we obtain

$$\bar{P} = -\frac{\bar{E}bh^2}{3a^2}\left(1 + \frac{2}{\lambda_t a} + \frac{2}{(\lambda_t a)^2}\right)^{-1} \tilde{U} \tag{16}$$

where $\bar{P} = P_1 + P_2$, $\tilde{U} = U_1 - U_2$, $\lambda_t = \sqrt{\frac{8K_t}{\bar{E}h}}$, and K_t is the tangential stiffness of the interface. Both K_n and K_t are assumed to be constants, independent of the separation rate or mode-mix, as was subsequently determined from the experiments.

Moreover, we find that

$$\bar{P} = \frac{\bar{E}bh^3\lambda_t^3}{\lambda_t^3\left(L^3 + 3a^3\right) + 9\lambda_t^2 a^2 + 9\lambda_t L + 9\lambda_t a - 9}\bar{\Delta} \tag{17}$$

where $\bar{\Delta} = \Delta_1 + \Delta_2$. It can be shown that Eqs. (15) and (17) recover Eqs. (6) and (7) at the limiting case of LEFM when $K_n, K_t \to \infty$.

Therefore, for a given crack length (a), the forces at the loading end (P_1 and P_2) are linearly related to the end displacements (Δ_1, Δ_2, U_1, U_2). The interfacial stiffnesses, K_n and K_t, can thus be determined from the measured forces and displacements before the crack starts to grow. Meanwhile, the tangential displacement and the rotation at the loading end of the upper beam can also be predicted as

$$U_1 = \frac{\tilde{U}}{2} - \frac{3\tilde{P}}{2\bar{E}bh^2\lambda_n^2}(\lambda_n a + 1)^2 \tag{18}$$

$$\Theta_1 = \frac{3\tilde{P}}{\bar{E}bh^3\lambda_n^2}(\lambda_n a + 1)^2 + \frac{3\bar{P}}{4\bar{E}bh^3\lambda_t^2}\left[\lambda_t^2\left(L^2 + 3a^2\right) + 6\lambda_t a + 6\right] \tag{19}$$

where $\tilde{U}$ is proportional to $\bar{P}$ by Eq. (16). Then, the tangential displacement and the rotation at the loading end of the lower beam are: $U_2 = U_1 - \tilde{U}$ and

$$\Theta_2 = \Theta_1 - \frac{6\tilde{P}}{\bar{E}bh^3\lambda_n^2}(\lambda_n a + 1)^2 \tag{20}$$

Correspondingly, the normal and tangential separations at the crack tip are obtained as:

$$\delta^*_n = \frac{6\tilde{P}}{\bar{E}bh^3\lambda_n^3}(\lambda_n a + 1) \tag{21}$$

$$\delta^*_t = -\frac{6\bar{P}}{\bar{E}bh^2\lambda_t^2}(\lambda_t a + 1) \tag{22}$$

By the beam on elastic foundation model, the normal and shear tractions at the crack tip are linearly proportional to the respective crack-tip displacement components. Then, the normal and shear components of J-integral are obtained as:

$$J_1 = \frac{3\left(\tilde{P}a\right)^2}{\bar{E}b^2h^3}\left(1 + \frac{1}{\lambda_n a}\right)^2 \tag{23}$$

$$J_2 = \frac{9(\bar{P}a)^2}{4\bar{E}b^2h^3}\left(1 + \frac{1}{\lambda_t a}\right)^2 \tag{24}$$

With Eqs. (23–24), the phase angle of mode-mix can be defined locally based on the components of the J-integral as discussed in Appendix A (Eq. A(1)), namely

$$\Psi_J = \tan^{-1}\left(\frac{\bar{\Delta}}{\tilde{\Delta}}\left(\frac{\sqrt{3}\lambda_t^2 a^2(\lambda_t a + 1)}{3(\lambda_t a + 1)^3 + \lambda_t^3 L^3 + 9\lambda_t L - 12}\right)\left(\frac{2(\lambda_n a + 1)^3 + 1}{(\lambda_n a)^2(\lambda_n a + 1)}\right)\right) \tag{25}$$

Again, it can be shown that, at the limiting case when $K_n, K_t \to \infty$, Eqs. (23–24) recover the energy release rates in Eqs. (3–4), and Eq. (25) recovers the nominal phase angle in Eq. (8).

4. Results and discussion

A total of 25 specimens (silicon/epoxy/silicon) were tested under a range of loading conditions. The values of the end displacement ratio (Δ_2/Δ_1) that were considered are: −1, 0.5, 0.7, 0.8 and 0.95. At each ratio, five rates ($\dot{\Delta}_1$) were prescribed at the upper loading point: 0.001, 0.005, 0.025, 0.125 and 0.625 mm/s.[3] The nominally mode I case ($\Delta_2/\Delta_1 = -1$) was the focus of the previous work (Yang et al., 2020) without considering the effect of mode-mix. In this section, we first present the data and related analyses for one particular mixed-mode condition ($\Delta_2/\Delta_1 = 0.8$ and $\dot{\Delta}_1 = 0.625$mm/s). Then, we discuss the effects of rate and mode-mix on the fracture of the silicon/epoxy interface.

4.1. Direct measurements and crack tip quantities

The direct measurements are summarized in Fig. 5 for one specimen with $\Delta_2/\Delta_1 = 0.8$ and $\dot{\Delta}_1 = 0.625$mm/s. The nominally applied displacements (Δ_1 and Δ_2) compare well with the DIC measurements (Fig. 5a). The close agreement between the two indicates that machine compliance was not an issue here. The reaction forces (P_1 and P_2), tangential displacements (U_1 and U_2), and rotations (Θ_1 and Θ_2) measured at the loading ends all initially increased linearly with time (Fig. 5 b-d), suggesting that the system was responding elastically, as expected from the beam on elastic foundation model (Section 3.4). At $t \approx 0.7$s, the measured forces (Fig. 5b), tangential displacements (Fig. 5c) and end rotations (Fig. 5d) became nonlinear, indicating the beginning of crack growth. Due to the asymmetry in the loading conditions, the reaction forces (Fig. 5b) behaved differently at the loading ends of the upper and lower beams. While the force on the upper beam started

[3] The applied displacement rates for the nominally mode I case were actually $2\dot{\Delta}_1$ as the opening rates at the loading ends.

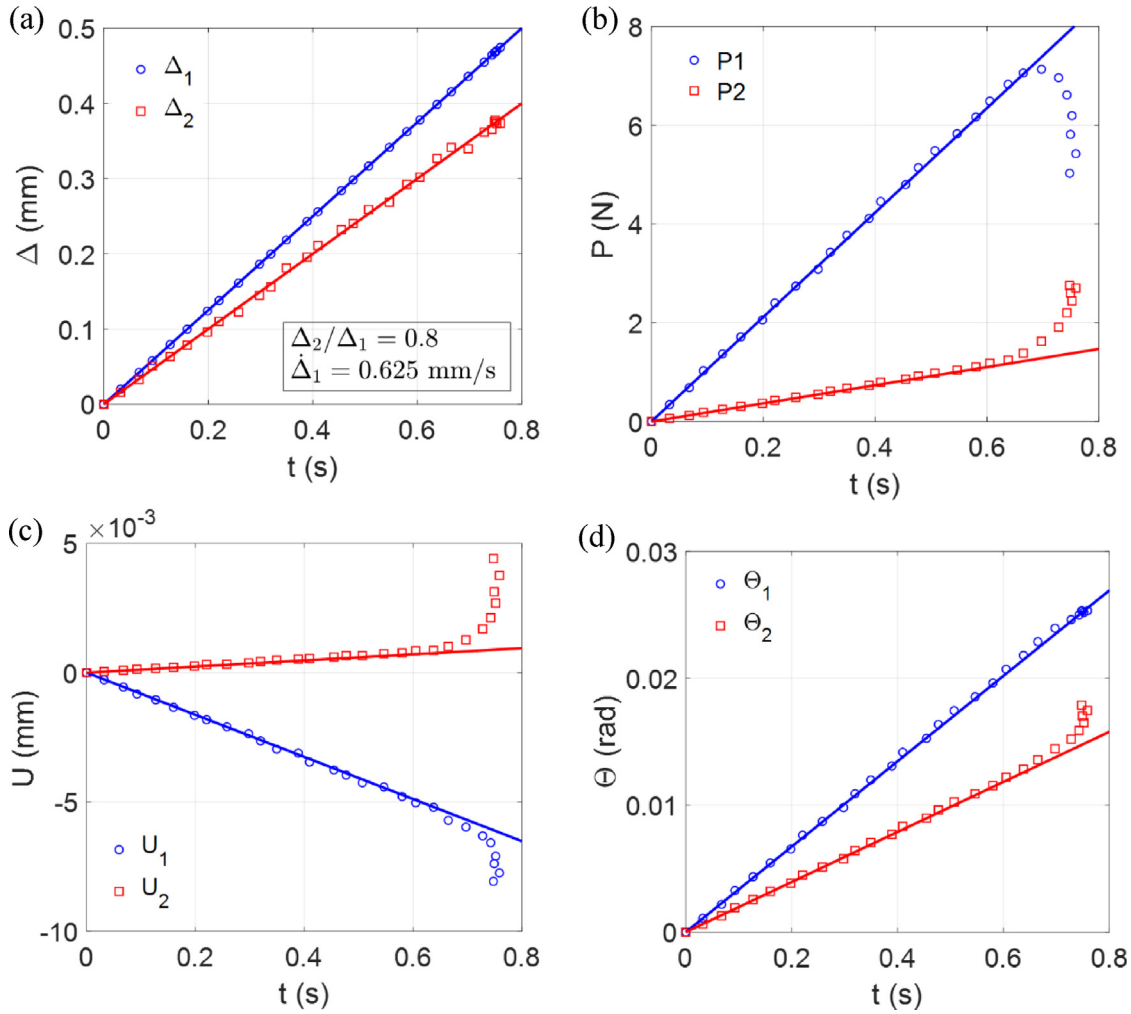

Fig. 5. Direct measurements for one mixed-mode specimen ($\Delta_2/\Delta_1 = 0.8$ and $\dot{\Delta}_1 = 0.625$ mm/s). (a) Applied normal displacements (lines) compared with DIC measurements (symbols); (b) Reaction forces at the loading ends; (c) Tangential displacements obtained by DIC; (d) Rotation angles obtained by DIC. In (b-d), the measurements (symbols) are compared to the beam on elastic foundation model (lines). The complete data set across all rates and mode-mixes appears in Supplementary Fig. S3-5.

dropping after its peak, the force on the lower beam started increasing at a higher rate. This was surprising (and will be discussed later) but signified a re-distribution of the total force on the upper and lower beams as the crack grew (hence change of mode-mix). Although the normal displacements were increased at a prescribed rate (Fig. 5a), the tangential displacements (Fig. 5c) exhibited an accelerating separation following initiation of crack growth. Meanwhile, the relative rotation ($\Theta_1 - \Theta_2$) decreased as the crack grew (Fig. 5d).

According to the beam on elastic foundation analysis (Section 3.4), we can fit the initially linear load–displacement responses (Fig. 6a and Fig. 6b) by Eqs. (15) and (16) using the initial crack length ($a_0 = 12$ mm) to determine the normal and tangential stiffness of the interface. In this case, we obtain $K_n = 5 \times 10^{12}$ N/m^3 and $K_t = 16 \times 10^{12}$ N/m^3. With these stiffness values, we calculate the reaction forces, tangential displacements and rotations at the loading ends by Eqs. (17–20), which compare closely with the measurements (Fig. 5, b-d) for the initially linear responses before crack growth started. In the past (Chow et al., 1979; Kanninen, 1973), the foundation stiffness was obtained from ratio of the tensile modulus and thickness of the epoxy layer, based on a simple strength of materials argument. Dillard et al. (2018) have recently provided a much deeper analysis of the complexity of the stress state in sandwich beams and its effect on assigning a foundation stiffness. In the present work, with the plane-strain modulus (~2.7 GPa) and thickness (~0.04 mm) of the epoxy, the normal stiffness by the simple analysis is 67.8×10^{12} N/m^3, much larger than the one extracted by the beam on elastic foundation analysis. Similarly, with the shear modulus (~0.9 GPa) for the epoxy, the tangential stiffness by the simple analysis is 22.4×10^{12} N/m^3, also larger than the value extracted by the beam on elastic foundation analysis. Nonetheless, the lower stiffness values obtained here suggest the presence of interfacial interactions that are more compliant than those of the bulk epoxy. This could be attributed to the formation of an interphase region, whose presence has been postulated (Vanlandingham et al., 1999) due to the migration of the amido amine hardener to the interface and a resultant, off-stoichiometric cure close to the interface.

Based on the measured force–displacement responses (Fig. 6a and 6b) and the extracted stiffness values, the beam on elastic foundation analysis was used to estimate the crack extension ($\Delta a = a - a_0$) following both Eqs. (15) and (16) (Fig. 6c). The results indicate that, within measurement uncertainty, the two equations yielded the same crack length over the entire experiment, implying that one crack front was shared by the normal and shear interactions, as noted by Wu et al. (2019).

By Eqs. (9) and (10), the normal and shear components of the J-integral were obtained directly from the measurements (Fig. 5)

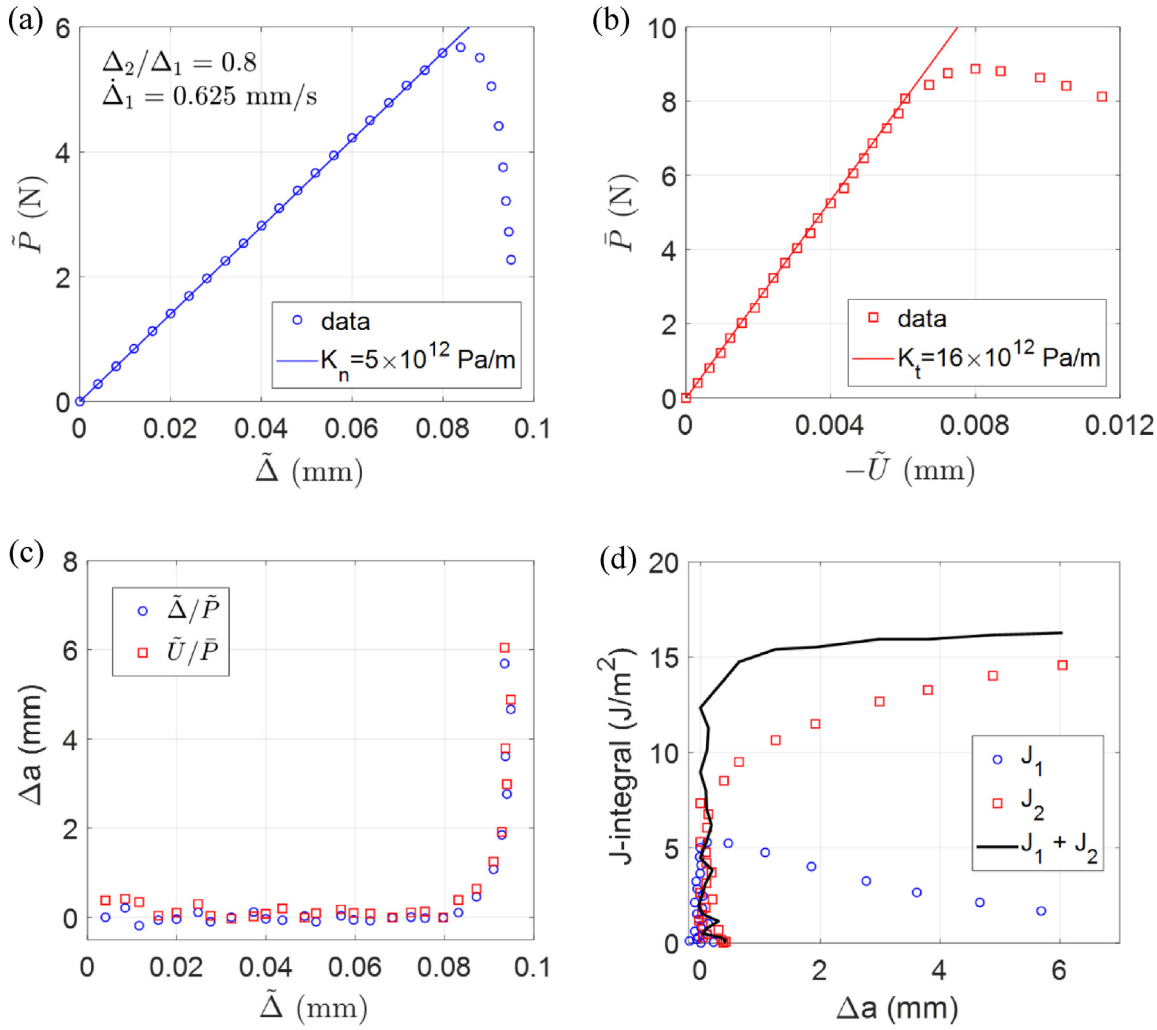

Fig. 6. (a) Force difference ($\tilde{P} = P_1 - P_2$) versus the normal separation ($\tilde{\Delta} = \Delta_1 - \Delta_2$) at the loading end, with the initially linear response fitted by Eq. (15); (b) Force combination ($\bar{P} = P_1 + P_2$) versus the tangential separation ($-U = U_2 - U_1$) at the loading end, with the initially linear response fitted by Eq. (16); (c) Crack extension estimated by Eq. (15) and Eq. (16); (d) J-integrals by Eqs. (9–10) versus the crack extension ($\Delta_2/\Delta_1 = 0.8$ and $\dot{\Delta}_1 = 0.625$ mm/s).

without relying on the assumption of any particular traction-separation relations or measurements of the crack length. The total J-integral ($J = J_1 + J_2$) is plotted versus the crack extension as the fracture resistance curve (R-curve) in Fig. 6d. Interestingly, while the total J-integral increases slightly as expected for a typical R-curve, the two components behave differently, with the normal component (J_1) decreasing and the shear component (J_2) increasing. The divergent behavior of the normal and shear components of the J-integral is tied to the variations of the loads, tangential displacements and rotations at the points of load application in each beam (Fig. 5 b-d), which results in a change of mode-mix during the crack growth. The relative uncertainty associated with the J-integral measurements was generally less than 0.1% (Appendix C).

Following Eqns. (11) and (12), the normal and tangential separations at the initial crack tip (with $a_0 = 12$ mm) were determined based on the remote measurements (Fig. 7). Generally, the relative uncertainty in the crack tip displacements was less than 2% (Appendix C). For comparison, based on the beam on elastic foundation analysis, Eqns. (23) and (24) were used to calculate the crack-tip separations using the extracted stiffness values, which are shown in Fig. 7 as straight lines, in good agreement with the data up to the point of crack growth. It is noted that there is relatively large scatter for the normal separation data (δ^*_{n0}) before the onset of crack growth, which is likely due to the relatively large error in the measurement of end rotations.

With this set of data and analyses, we have established the values of stiffness of the normal and shear interaction (K_n and K_t), the R-curve for crack growth (Fig. 6d), and the local separations at the initial crack tip (Fig. 7). Of particular interest is the critical condition for the onset of crack growth, which occurred at $\tilde{\Delta} = 0.08$ mm (Fig. 6c). Correspondingly, the critical J-integral is found to be $J = 12.3$ J/m^2, with two components, $J_1 = 5$ J/m^2 and $J_2 = 7.3$ J/m^2; the critical separations at the initial crack tip are: $\delta^*_{n0} = 1.4$ μm and $\delta^*_{t0} = 0.95$ μm, while the critical tractions (strengths) are: $\sigma^*_{n0} = K_n\delta^*_{n0} = 7.0$ MPa and $\sigma^*_{t0} = K_t\delta^*_{t0} = 15.2$ MPa. As will be discussed later, the critical J-integral for the onset of crack growth depends on the local separation rate (Section 4.2) and the mode-mix (Section 4.3). Upon crack growth, both the local separation rate and the mode-mix change, leading to the noted changes in the components of the J-integral (Fig. 6d).

4.2. Loading rate effect

The steps described above were followed for each specimen that was tested, and the data for all specimens is presented in Sup-

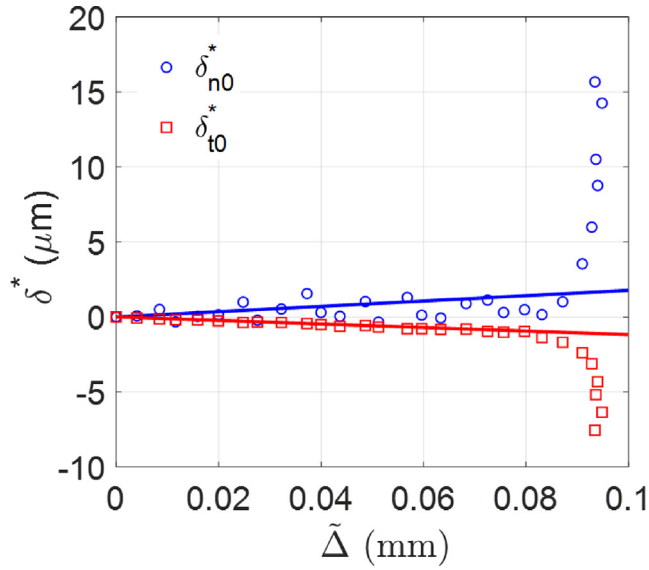

Fig. 7. Normal and tangential separations at the initial crack tip versus applied displacement (data denoted by symbols and the beam on elastic foundation analyses denoted by lines with matched colors) ($\Delta_2/\Delta_1 = 0.8$ and $\dot{\Delta}_1 = 0.625$ mm/s).

plementary Materials (Figs. S3-S9). In this section we focus on the effects of loading rate for the mixed-mode specimens with the same applied displacement ratio of $\Delta_2/\Delta_1 = 0.8$. According to Eq. (8), the nominal phase angle at the initial crack tip is 42°, while it is higher (~65°) after considering the epoxy layer as shown in Fig. 4.

It is found that the values of the stiffness of the normal and shear interaction (K_n and K_t) are rate independent, signified by the same slopes in the initially linear responses for all five rates (Fig. 8). Previously we have shown that the normal interaction stiffness was rate independent under the nominally mode-I conditions (Yang et al., 2020).

The crack lengths are extracted from the remote measurements (Fig. 9a) and the R-curves with the total J-integral are shown in Fig. 9b. Clearly, the critical J-integral for the onset of crack growth decreases as the loading rate decreases, similar to the previous results for the nominally mode-I cases (Yang et al., 2020). Since the force–displacement responses are linear up to the critical point with the same stiffness, the ratio between the normal and shear components of the J-integral is rate independent before crack growth. For $\Delta_2/\Delta_1 = 0.8$, we obtain $J_2/J_1 = 1.46$, which yields a local phase angle of 50° for the mode-mix by Eq. (A1). Upon crack growth, however, the ratio J_2/J_1 increases, leading to an increasing phase angle (Fig. A1b). Meanwhile, the crack growth rate also increases (Fig. 9a), which may lead to increase in the local separation rate at the crack tip. The increases in the phase angle of mode-mix and the crack growth rate (or local separation rate) both contribute to the increase in the total J-integral. To examine the two effects separately, we limit our focus to the critical condition for the onset of crack growth, for which the mode-mix is controlled by the applied displacement ratio (Δ_2/Δ_1) and the local separation rate is controlled by the loading rate ($\dot{\Delta}_1$).

Based on the beam on elastic foundation model, the local separation rate at the initial crack tip can be estimated by Eqs. (21) and (22) along with Eqs. (15) and (17), so that

$$\dot{\delta}^*_{n0} = \frac{3(1+\lambda_n a_0)}{2(1+\lambda_n a_0)^3 + 1}\dot{\tilde{\Delta}} \tag{26}$$

$$\dot{\delta}^*_{t0} = \frac{6\lambda_t h(1+\lambda_t a_0)}{\lambda_t^3\left(L^3 + 3a_0^3\right) + 9\lambda_t^2 a_0^2 + 9\lambda_t L + 9\lambda_t a_0 - 9}\dot{\tilde{\Delta}} \tag{27}$$

For the mixed-mode specimens with $\Delta_2/\Delta_1 = 0.8$, we obtain $\dot{\delta}^*_{n0} = 0.0035\dot{\Delta}_1$ and $\dot{\delta}^*_{t0} = 0.0024\dot{\Delta}_1$, with a ratio between the shear and normal components, $\dot{\delta}^*_{t0}/\dot{\delta}^*_{n0} = 0.68$, which remains constant up to the onset of crack growth. The corresponding critical values of the J-integral are shown as a function of the vectorial separation rate, $\dot{\delta}^*_0 = \sqrt{\left(\dot{\delta}^*_{n0}\right)^2 + \left(\dot{\delta}^*_{t0}\right)^2}$, in Fig. 10a. The critical values of the normal and shear components of the J-integral are shown as functions of the corresponding components of the local separation rate. The corresponding critical traction components can be obtained as: $\sigma_{nc} = \sqrt{2K_n J_{1c}}$ and $\sigma_{tc} = \sqrt{2K_t J_{2c}}$, as shown in Fig. 10b. Evidently, at the same mode-mix, the critical values of the J-integral and its components all increase monotonically with the local separation rate. Interestingly, the critical value of the J-integral appears to be more sensitive to the separation rate for relatively low rates and becomes less sensitive at the higher rates, which is qualitatively consistent with the prediction by a rate-dependent cohesive zone model based on the thermally activated chain scission mechanism (Yang et al., 2020), although the previous model was developed under nominally mode-I fracture conditions. The normal and shear strengths naturally display similar trends (Fig. 10b) as the critical values of the J-integral components. At this mode-mix, the shear strength is consistently higher for all separation rates and the values of both components are well below the corresponding strengths of the bulk epoxy. Furthermore, the normal strengths are lower than those that were obtained under nominally mode I conditions (Yang et al., 2020), but could certainly be consistent with a rate-dependent cohesive zone model under mixed-mode conditions, which is left for future consideration.

4.3. Effect of mode-mix

In this section, we discuss the effect of mode-mix due to different ratios of the applied displacements (Δ_2/Δ_1) at the loading end of the specimens. Following the same steps in Sections 4.1 and 4.2, we determine the values of the stiffness of the normal and shear interactions (K_n and K_t), the R-curves for crack growth, and the local separations at the initial crack tip as well as the critical condition for onset of crack growth in each specimen. We are also interested in the combined effect of the mode-mix and loading rate during crack growth. The original data for all specimens is presented in Supplementary Materials (Figs. S3-S5), and the results from the data analysis are shown in Figs. S6-S9.

The first step is to determine the values of the stiffness of the normal and shear interactions (K_n and K_t) from the initially linear responses. Both K_n and K_t are not only rate independent (Fig. 8) but also independent of mode-mix (Fig. 11 and Figs. S6-S7 in Supplementary Materials, including the nominally mode-I cases). This is remarkable as the stiffness values appear to be robust properties of the silicon/epoxy interface over a wide range of mode-mix and loading rate. On the other hand, the critical condition for onset of crack growth does depend on the mode-mix. As shown in Fig. 12a for $\dot{\Delta}_1 = 0.625$ mm/s with different applied displacement ratios (Δ_2/Δ_1), the crack growth started at different applied separation ($\tilde{\Delta} = \Delta_1 - \Delta_2$), which indicates different critical values of the normal components of the J-integral (J_{1c}). As the ratio Δ_2/Δ_1 increases, J_{1c} decreases (Fig. 13). Meanwhile, the ratio of the tangential to the normal components of the J-integral, J_2/J_1, increases and the critical tangential component (J_{2c}) increases. The total J-integral is shown in Fig. 12b as a function of the crack extension for each specimen. The critical total J-integral ($J_c = J_{1c} + J_{2c}$) is com-

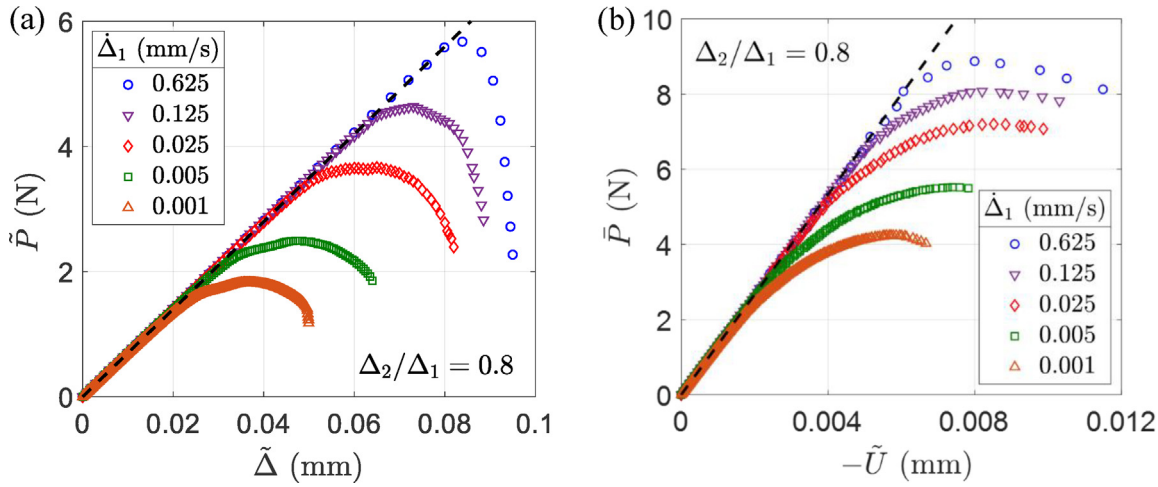

Fig. 8. (a) Force difference ($\tilde{P} = P_1 - P_2$) versus the normal separation ($\tilde{\Delta} = \Delta_1 - \Delta_2$) at the loading end; (b) Force combination ($\bar{P} = P_1 + P_2$) versus the tangential separation ($-\tilde{U} = U_2 - U_1$) at the loading end, under five rates with $\Delta_2/\Delta_1 = 0.8$. The earlier derived values of stiffness of the normal and shear interactions (K_n and K_t) are used to obtain all of the initially linear responses, shown as the dashed lines. The complete data set across all separation rates and mode-mixes appears in Supplementary Figs. S6 and S7.

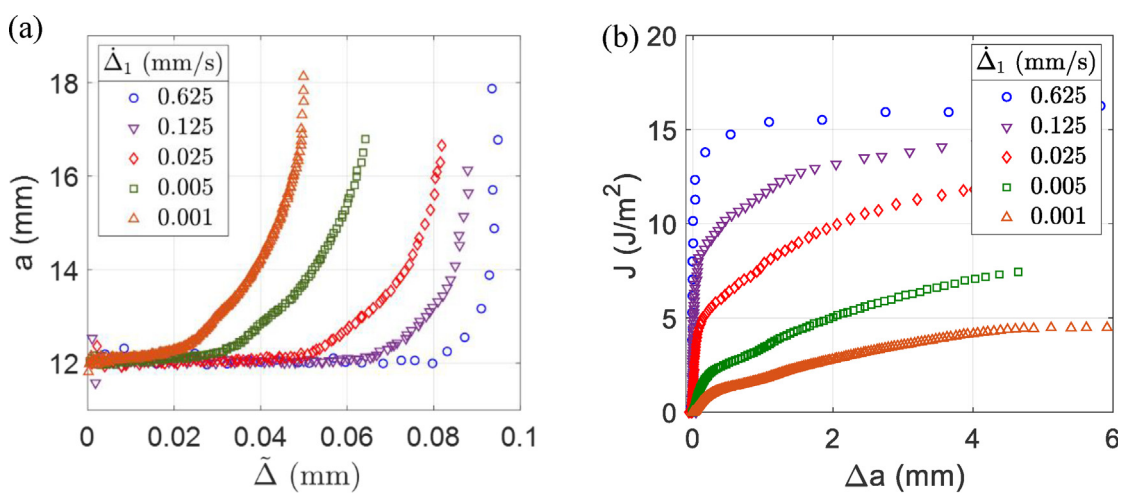

Fig. 9. (a) Crack length extracted from measurements versus the applied displacement; (b) J-integral versus the crack extension, for specimens tested at different loading rates and $\Delta_2/\Delta_1 = 0.8$. Crack length and J-integral data across all separation rates and mode-mixes appears in Supplementary Figs. S8 and S9, respectively.

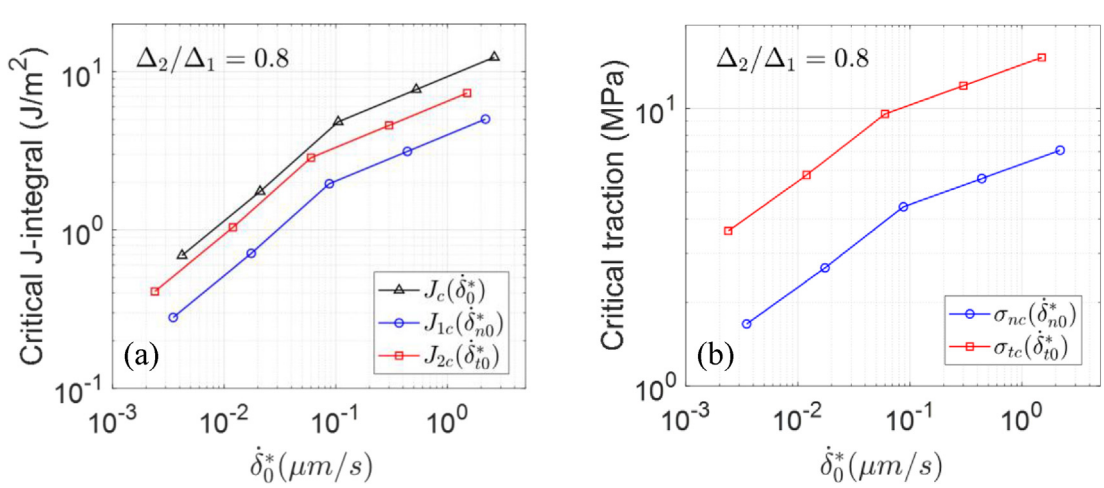

Fig. 10. (a) The critical J-integral and (b) the critical traction components versus the local separation rate at the initial crack tip, for specimens tested at $\Delta_2/\Delta_1 = 0.8$. Critical J-integral and traction data across all separation rates and mode-mixes appears in Figs. S10 & S11, respectively.

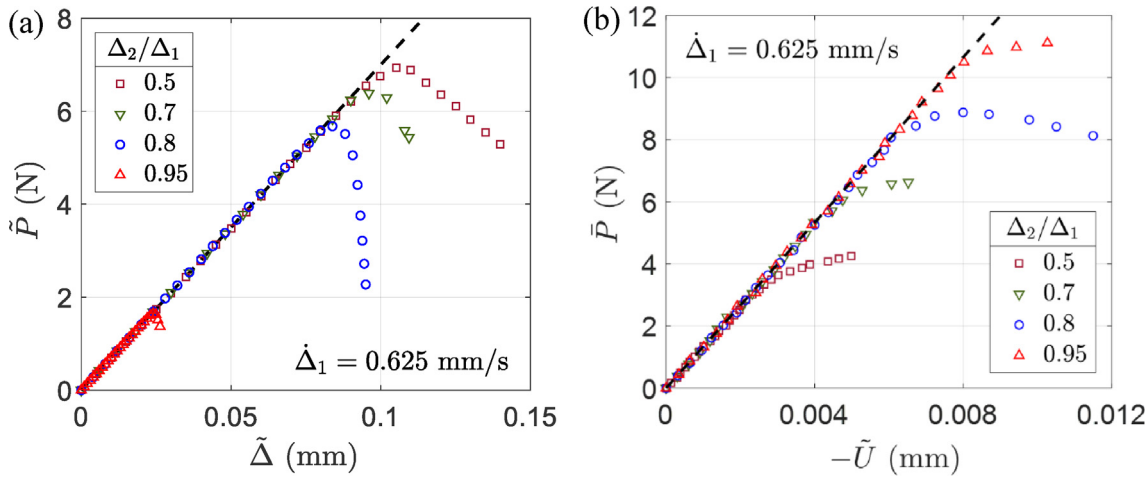

Fig. 11. (a) Force difference ($\tilde{P} = P_1 - P_2$) versus the normal separation ($\tilde{\Delta} = \Delta_1 - \Delta_2$) at the loading end and (b) force combination ($\bar{P} = P_1 + P_2$) versus the tangential separation ($-\tilde{U} = U_2 - U_1$) at the loading end, with different ratios of the applied displacements (Δ_2/Δ_1) and $\dot{\Delta}_1 = 0.625$ mm/s. The previously determined values of the normal and shear interactions (K_n and K_t) are used to obtain the initially linear responses, shown as the dashed lines.

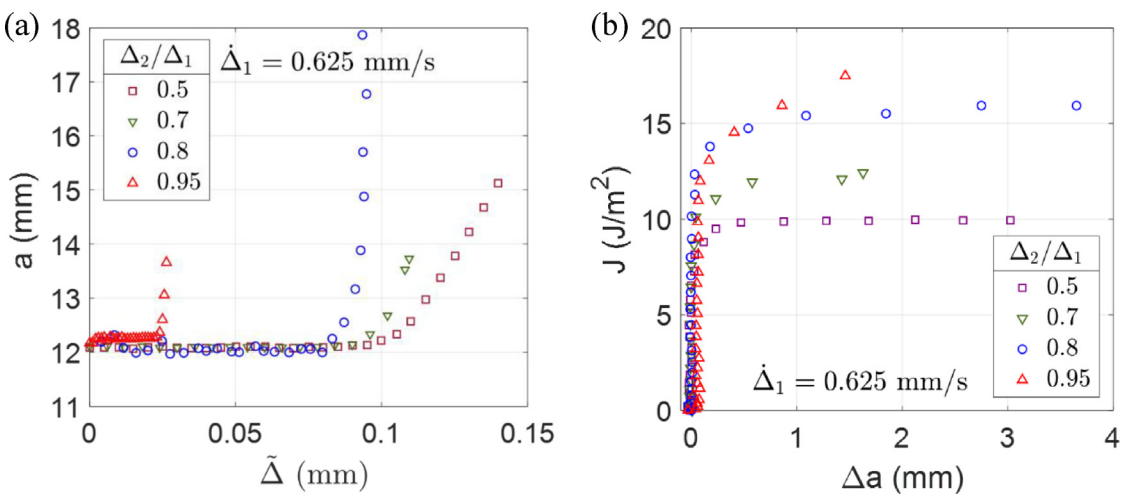

Fig. 12. (a) Crack length extracted from measurements versus the applied displacement; (b) J-integral versus the crack extension, for specimens tested at different mode-mixes with $\dot{\Delta}_1 = 0.625$ mm/s.

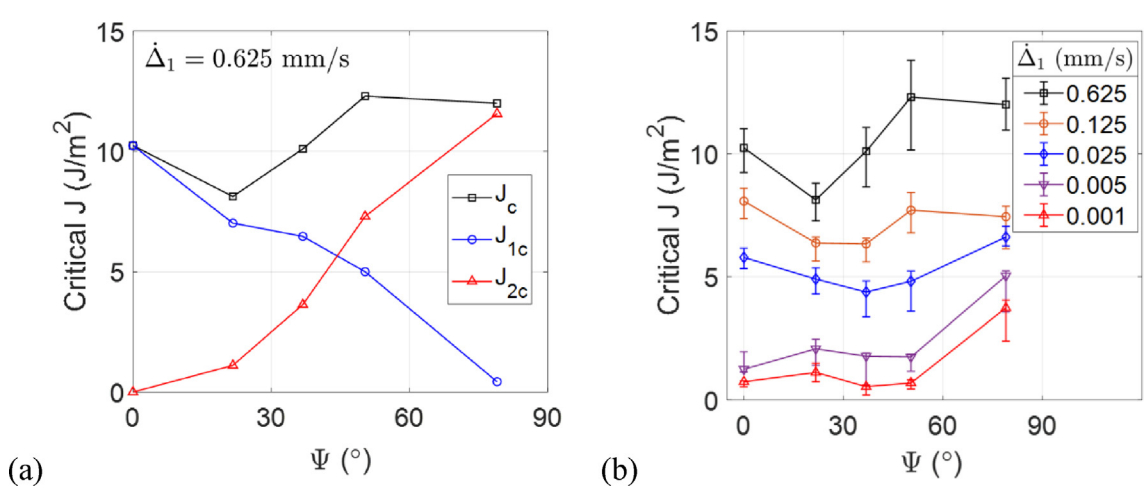

Fig. 13. (a) The critical J-integral as a function of the phase angle of mode-mix for specimens subject to the same applied displacement rate ($\dot{\Delta}_1 = 0.625$ mm/s) except for the nominally mode I case for which the applied displacement rate was half of 0.625 mm/s; (b) The variation of the critical values of the J-integral for the onset of crack growth as a function of phase angle and the rate of the displacement applied to the upper beam.

monly expected to increase with increasing mode-mix. However, it may also depend on the local separation rates at the initial crack tip. For the specimens with the same applied displacement rate (e.g.,$\dot{\Delta}_1 = 0.625$ mm/s) but with different displacement ratios (Δ_2/Δ_1), the local separation rates at the initial crack tip are different in both the normal and tangential directions. Interestingly, as the ratio Δ_2/Δ_1 increases, it is found that the local separation rate increases in the tangential direction ($\dot{\delta}^*_{t0}$) but decreases in the normal direction ($\dot{\delta}^*_{n0}$), while the vectorial separation rate ($\dot{\delta}^*_0$) decreases. Consequently, the effect of mode-mix in these specimens is coupled with the rate effect even at the initial crack tip.

As shown in Fig. 13a, the critical J-integral (J_c) appears to depend on the local phase angle ($\Psi_J = \tan^{-1}\sqrt{J_2/J_1}$) non-monotonically under the same applied displacement rate ($\dot{\Delta}_1 = 0.625$). This can be attributed to the combined effects of mode-mix and local separation rates: while the normal component (J_{1c}) decreases monotonically with increasing mode-mix and decreasing normal separation rate ($\dot{\delta}^*_{n0}$), the tangential component (J_{2c}) increases monotonically with increasing mode-mix and increasing tangential separation rate ($\dot{\delta}^*_{t0}$). Note that, for the nominally mode I case ($\Delta_2/\Delta_1 = -1$ and $\Psi \approx 0^\circ$), the applied displacement rate was half of 0.625 mm/s. Due to the rate effect, the critical J-integral would be higher than that shown in Fig. 13a if the same displacement rate ($\dot{\Delta}_1 = 0.625$ mm/s) were applied for the nominally mode I case, while the trend remains the same.

The values of the critical values of the J-integral for all the phase angles and applied displacement rates that were considered are shown in Fig. 13b. Although the values clearly increase with increasing applied displacement rate for all values of phase angle, there is no clear trend to the data as a function of phase angle for each applied displacement rate. The uncertainty in the critical values to the J-integral is tied to the uncertainty in assigning the onset of crack growth (see Figs. 9a and 12a), which is much greater than the relative error of the J-integral measurements themselves (Eqns. (9–10)) as discussed in Appendix C. Even so, the error bars do nothing to change the observation that there is no clear trend to J_c with phase angle. The onset of crack growth is sensitive to variations in interfacial conditions from specimen to specimen, but this was not addressed in the current study. More weight is usually placed on the steady state values of the J-integral than those at initiation as this is less sensitive to specimen to specimen variability. However, it was not possible to separate out rate and phase angle effects on steady state propagation as the cohesive zone developed when using the current loading configuration.

The values of the normal and shear components of the critical J-integral for the onset of crack growth in all specimens are shown in Fig. 14. For each mode-mix, both components increase monotonically with the crack-tip separation rate. The largest value of J_{1c} occurred under nominally mode I conditions at the highest separation rate, while the same was true for J_{2c} under nearly mode II conditions (also Fig. S10). Moreover, as the applied displacement ratio (Δ_2/Δ_1) increases, the phase angle of mode-mix increases, and as a result, the shear component of the critical J-integral increases, while the normal component decreases. However, for the cases of nominally mode-I fracture ($\Delta_2/\Delta_1 = -1$), the two specimens with the lowest rates appear to be outliers, falling below the mixed-mode cases at similar rates. Nevertheless, the dependence of the normal component (J_{1c}) on the mode-mix appears to be less significant than the shear component (J_{2c}) except for the cases of the highest phase angle ($\Delta_2/\Delta_1 = 0.95$). As a result, the total critical J-integral ($J_c = J_{1c} + J_{2c}$) generally increases with the separation rate and the mode-mix, although the two effects could be coupled as the mode-mix changes via the applied displacement ratio (Δ_2/Δ_1). The mixed-mode fracture criterion in Eq. (1) could be extended for rate-dependent fracture with the mode-I and mode-II toughness values, Γ_I and Γ_{II}, depending on the normal and tangential separation rates, respectively. However, such an extension does not seem to capture the results shown in Fig. 14. Alternatively, the rate-dependent cohesive zone models proposed previously for the mode-I fracture (Yang et al., 2020, 2019) may be extended to the mixed-mode cases by considering a damage evolution process depending on both the normal and tangential separations. Such a model would also be useful to predict the subsequent crack growth, where both the separation rate and mode-mix may change simultaneously along the interface and the damage/fracture processes are generally history dependent.

The strength values were a function of both rate and mode-mix (Fig. S11) with the maximum normal strength (~10 MPa) occurring under nominally mode I condition at the highest separation rate. Nearly mode II conditions resulted in the maximum shear strength (~20 MPa) at the highest separation rate. Both strength values were lower than the corresponding yield strengths of the bulk epoxy, suggesting that dissipation effects were confined to the interphase region. Sills and Thouless (2013) defined bimaterial length scales for the cohesive zone size associated with normal and shear tractions. Considering the nominally mode I and nearly mode II cases

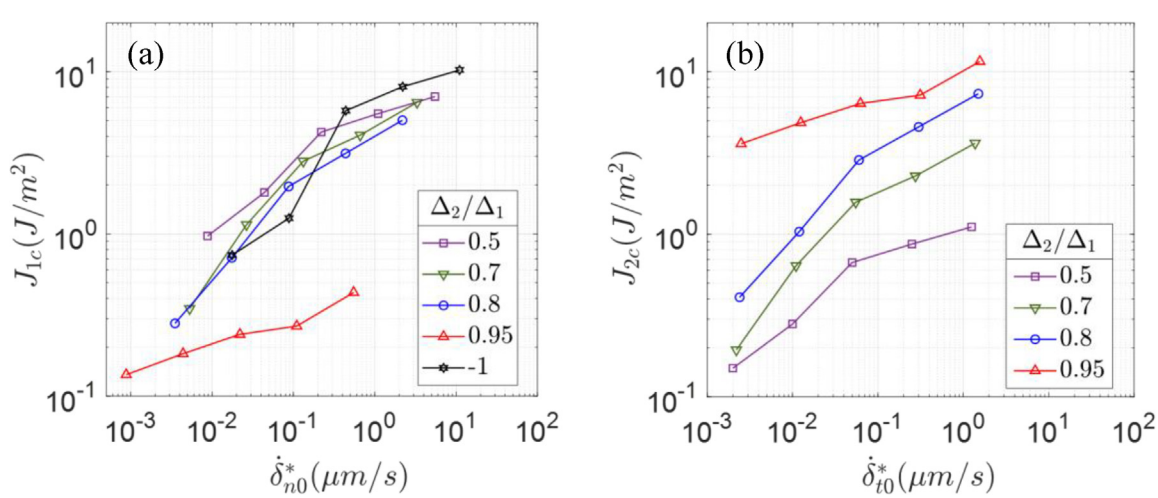

Fig. 14. (a) Normal and (b) shear components of the critical J-integral versus corresponding components of the crack tip separation rate under different mode-mix conditions.

presented here at the highest separation rates, the normal and shear cohesive lengths were 20 and 7.5 times the beam thickness, respectively. This means that large scale bridging was in effect at both extremes and provides further insight into the complications that are induced by applying asymmetric end displacements, despite the findings of Pappas and Botsis (2019) for adhesively bonded joints loaded by end displacements or moments.

The components of J-integral obtained directly from the remote measurements by Eqs. (9–10) follow a continuous path before and after crack growth as shown in Fig. 15a for the four mixed-mode specimens loaded at the fastest displacement rate ($\dot{\Delta}_1 = 0.625$ mm/s). For each specimen, the two components increase proportionally before the onset of crack growth, as predicted by the beam on elastic foundation analysis with a constant initial crack length. Upon crack growth, the path deviates with an increasing ratio between J_2 and J_1, indicating a change of mode-mix. By Eq. (A1), the phase angle of the mode-mix can be calculated (Fig. A1b) and compared with the nominal phase angle from Eq. (8). While the trend is similar in all cases, the phase angle based on the J-integral components is generally higher than the nominal phase angle, which may be attributed to the finite interaction stiffness values (K_n and K_t) at the interface. It should be noted that the path followed by the components of the J-integral also depends on the applied displacement rate, especially during crack growth. While the local separation rate remains constant at the initial crack tip until the onset of crack growth, the separation displacements at the new crack tip may not follow a constant rate. We calculate the normal and shear components of the crack-tip displacements (Fig. 15b) by Eqs. (11–12), where the crack length is estimated from the beam on elastic foundation analysis (Eqs. (15–16)). The paths followed by the components of the crack-tip displacement are similar to those taken by the components of J-integral. We note that, during crack growth, the location of the crack tip changes and thus the crack-tip displacements are taken at different locations along the interface. A more detailed analysis is required to determine the local separation rate at each location, which is possible by the mixed-mode beam on elastic foundation model. However, since the local separation rate is generally not a constant (except for the initial crack tip), a history-dependent fracture criterion is needed to predict the crack

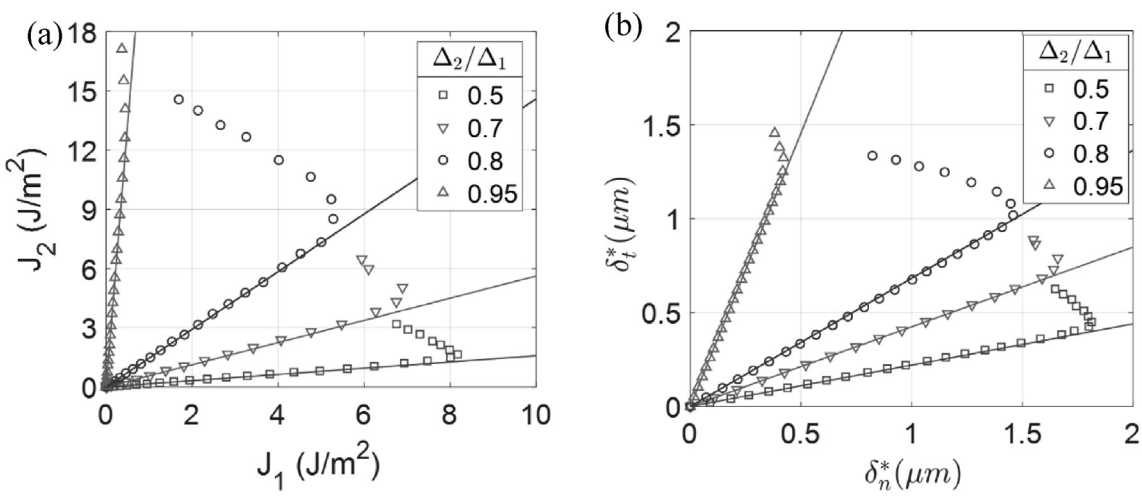

Fig. 15. Loading path by (a) J-integrals and (b) crack tip displacements, at five prescribed displacement ratios a global rate of 0.625 mm/s. Lines are predicted by the beam on elastic foundation model using the initial crack length.

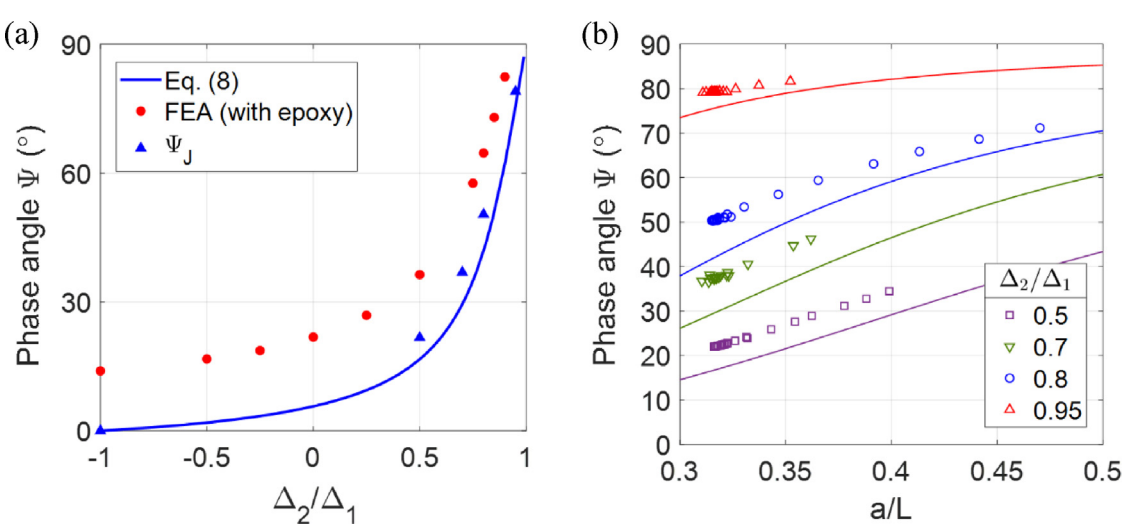

Fig. A1. (a) Local phase angles ($\Psi_J = \tan^{-1}\sqrt{J_2/J_1}$) at the initial crack tip compared with the nominal phase angles predicted by Eq. (8) and finite element analysis (with epoxy); (b) Variation in the local phase angle during crack growth under mixed-mode conditions at four prescribed displacement ratios. The nominal phase angles predicted by Eq. (8) are shown as lines.

growth. As noted earlier, a mixed-mode damage evolution process may be considered to extend the rate-dependent and history-dependent cohesive zone models (Yang et al., 2020, 2019) from mode-I to the mixed-mode cases, which is however beyond the scope of the present work.

5. Conclusions

This paper presents a novel design for a dual-actuator loading device and its application in characterizing the rate dependent fracture for a silicon/epoxy interface under mixed-mode loading conditions. The rate effect was examined by controlling the global transverse displacement rate at the loading end. Different mixed-mode fracture conditions were achieved by varying the displacement ratio between the upper and lower beams, which is more convenient than working with a series of asymmetric specimens that satisfy the balance condition. Direct extraction of the normal and shear components of the J-integral and the crack-tip displacements using only far-field measurements at any mode-mix was enabled by identically satisfying a balance condition based on a beam interaction analysis.

A mixed-mode beam on elastic foundation analysis was then used to determine the interfacial stiffness and, subsequently, the onset of crack growth during each experiment. The stiffness of the normal and shear interactions between the epoxy and silicon was found to be independent of the separation rate and mode-mix. The interfacial stiffness values were lower than the counterparts based on the bulk tensile and shear stiffness of the epoxy layer. The analysis, coupled with the fact that stiffness of both interactions was independent of rate and mode-mix, also allowed the crack growth to be tracked in order to determine the critical values of the J-integral for its onset. For each mode-mix, the critical J-integral and the corresponding interfacial strength both increased with increases in the separation rate. This increase is in spite of the glassy nature of the bulk epoxy and suggests the presence of an interphase region in the epoxy adjacent to the silicon.

The change of mode-mix with the applied displacement ratio was accompanied by the change of the local separation rate at the crack tip, leading to non-monotonic change in the critical J-integral, although its normal and tangential components each changes monotonically in opposite trends. Under uneven, transverse end-displacements, both the local separation rate and phase angle of mode mix vary with crack length, which leads to a variation of interfacial properties as the crack grows that cannot be separately attributed to either effect. Loading configurations that apply uneven bending moments to each adherend (Jacobsen and Sørensen, 2001; Lindhagen and Berglund, 2000; Pappas and Botsis, 2019; Sørensen and Jacobsen, 2009, 1998) do not suffer from changing mode-mix as the crack grows. However, rate effects are still expected to raise issues in any attempts at direct extraction of traction-separation relations. This work has demonstrated that the direct approach cannot be used in the all-embracing extraction of rate dependent traction-separation relations due to the fact that the local rate is constantly evolving with crack extension. The silicon/epoxy interface considered in the present work provided some relief in this respect because the response prior to crack initiation was independent of separation rate. Ultimately, future efforts that focus on developing intrinsically rate dependent cohesive zone models with mixed-mode interactions are recommended to better understand the rate dependent fracture of such interfaces under mixed-mode loading conditions.

Declaration of Competing Interest

The authors declare that they have no known competing financial interests or personal relationships that could have appeared to influence the work reported in this paper.

Acknowledgments

The authors gratefully acknowledge the financial support of this work by the Semiconductor Research Corporation (SRC Task ID: 2886.001). The senior authors (RH and KML) are honored to have this paper included in the special edition celebrating the 70th birthday of Stelios Kyriakides, our colleague and longtime friend (KML). Stelios is a leader in so many ways and an inspiration to most of us, but what I value above all is his friendship and companionship.

Appendix A. Various mode-mix definitions

The phase angle of mode-mix for interfacial fracture may be defined either by linearly elastic fracture mechanics (LEFM) (Hutchinson and Suo, 1992; Rice, 1988) or by cohesive zone models. Specifically, for the laminated beam specimens considered in the present study, a nominal mode-mix can be defined based on LEFM without considering the thin epoxy layer, as given by Eq. (8). The presence of a thin epoxy layer between the two silicon beams leads to an elastic mismatch at the interface and a shift of the phase angle (Fig. 4) compared to the corresponding homogeneous system. Moreover, when there is an elastic mismatch, an arbitrary length scale is required to define the mode-mix by LEFM. Here we used the thickness of the epoxy layer as the length scale for the phase angle. A finite element model was used to calculate the phase angles in Fig. 4, similar to those in previous works (Wu et al., 2016, 2019).

For cohesive zone modeling, the local mode-mix at the crack tip can be defined based on the components of J-integral, the separation displacements, or the tractions at the crack tip as follows:

$$\Psi_J = \tan^{-1}\left(\sqrt{\frac{J_2}{J_1}}\right) \tag{A1}$$

$$\Psi_\delta = \tan^{-1}\left(\frac{\delta_t^*}{\delta_n^*}\right) \tag{A2}$$

$$\Psi_\sigma = \tan^{-1}\left(\frac{\sigma_t^*}{\sigma_n^*}\right) \tag{A3}$$

These definitions may yield different phase angles for the local mode-mix, and in general also differ from the nominal phase angle by LEFM (Eq. (8)). In the present study we adopt Eq. (A1) for the local mode-mix, which can be determined directly from the remote measurements based on Eqs. (9–10) and predicted by Eq. (25), based on the beam on elastic foundation analysis.

The phase angles at the initial crack tip ($a_0 = 12$ mm) are shown in Fig. A1a as a function of the applied displacement ratio (Δ_2/Δ_1), comparing the nominal phase angles predicted by Eq. (8) with those obtained from the finite element analysis (FEA) including the epoxy layer and those based on the remote measurements. At each applied displacement ratio (Δ_2/Δ_1), the components of J-integral were obtained from Eqs. (9–10) using the measurements that were made at the loading ends of the specimen. The phase angles obtained by using Eq. (A1) lie in between of the other two

phase angles, independent of the applied displacement rate ($\dot{\Delta}_1$). In the case of symmetric loading ($\Delta_2/\Delta_1 = -1$), the responses as measured in terms of the reaction forces (P_1 and P_2), tangential displacements (U_1 and U_2) and end rotations (Θ_1 and Θ_2) are essentially symmetric (Fig. S3a), resulting in nearly zero tangential component for the J-integral and thus a nearly zero phase angle.

In addition, the mode-mix for the laminated beam specimen depends on the crack length (Fig. A1b) for a given displacement ratio (Δ_2/Δ_1). From the simple beam analysis that ignored the presence of the epoxy layer (Eq. (8)), the nominal phase angle increases with increasing crack length, except for the pure mode-I and mode-II cases. Similarly, based on the components of the J-integral obtained from the remote measurements, the local mode-mix based on Eq. (A1) increases as the crack grows, except for the case of symmetric loading ($\Delta_2/\Delta_1 = -1$) where the phase angle remains nearly zero. At the other limit ($\Delta_2/\Delta_1 = 0.95$), the phase angle of the local mode-mix changes slightly and remains close to 80° as the nearly mode II condition. For the three intermediate displacement ratios, the local mode-mix changes considerably during crack growth. Moreover, it was found that the mode-mix is rate independent at the initial crack tip and during crack growth, as can be expected from Eq. (25) due to the rate-independence of both stiffness components (K_n, K_t) of the silicon/epoxy interface. Note that the mode-mix does not vary with crack length in a dual actuator device operating under load control (see Eqs. (3–4)). However, crack growth is likely to be unstable under load control.

Appendix B. A beam on elastic foundation model with normal and shear interactions

A beam on elastic foundation model was presented previously by Gowrishankar et al. (2012) for normal interactions only. Here, we extend the model to include both the normal and shear interactions at the interface. Assume the tractions at the interface are linearly related to the respective separations with two independent spring constants, normal stiffness K_n and shear stiffness K_t, namely

$$\sigma_n = K_n \delta_n \tag{B1}$$

$$\sigma_t = K_t \delta_t \tag{B2}$$

For the symmetric double cantilever beam specimen (Fig. 2), the governing equations for the normal and shear interactions are decoupled (Wu et al., 2019):

$$\frac{\bar{E}h^3}{24}\frac{d^4\delta_n}{dx^4} + \sigma_n = 0 \tag{B3}$$

$$\frac{\bar{E}h}{8}\frac{d^2\delta_t}{dx^2} - \sigma_t = \frac{3\bar{P}}{4bh} \tag{B4}$$

where $\bar{P} = P_1 + P_2$.

With the linear traction-separation relation in Eq. (B1), the governing equation for the normal interactions (Eq. B(3)) has been solved by Gowrishankar et al. (2012), yielding a linear relation between the force difference $\left(\tilde{P} = P_1 - P_2\right)$ and the normal separation at the loading ends $\left(\tilde{\Delta} = \Delta_1 - \Delta_2\right)$, as given in Eq. (15). Moreover, the normal components of J-integral and the crack-tip displacement can be obtained from Eqs. (21) and (23), respectively.

Similarly, the governing equation for the shear interactions (Eq. B(4)) can be solved with the linear relation in Eq. (B2). First, noting that $\sigma_t = 0$ for $-a < x < 0$ (the cracked part), we solve Eq. (B4) with the boundary conditions at the loading end, $\delta_t(x = -a) = U$ and $\delta_t'(x = -a) = 0$, and obtain the tangential separation for the cracked part as

$$\delta_t(x) = \tilde{U} + \frac{3\bar{P}a^2}{\bar{E}bh^2}\left(1 + \frac{x}{a}\right)^2 \tag{B5}$$

where $\tilde{U} = U_1 - U_2$ is the tangential separation at the loading end ($x = -a$). Therefore, the tangential displacement at the crack tip ($x = 0$) is given by Eq. (12), regardless of the traction-separation relation ahead of the crack tip.

Next, for $x > 0$, we solve Eq. (B4) with the linear relation in Eq. (B2) and obtain

$$\delta_t(x) = A\sinh(\lambda_t x) + B\cosh(\lambda_t x) + \frac{3\bar{P}}{4K_t bh} \tag{B6}$$

where $\lambda_t = \sqrt{\frac{8K_t}{\bar{E}h}}$. Applying the continuity conditions for δ_t and δ_t' at $x = 0$ with Eqs. (B5) and (B6), we obtain

$$A = \frac{6a}{\bar{E}bh^2\lambda_t}\bar{P} \tag{B7}$$

$$B = \tilde{U} + \left(\frac{3a^2}{\bar{E}bh^2} + \frac{3}{4K_t bh}\right)\bar{P} \tag{B8}$$

Moreover, at the clamped end ($x = L - a$), we must have $\delta_t = 0$, which requires that

$$\bar{P} = \frac{\bar{E}bh^2}{6a^2}\left(\frac{1}{2} + \frac{1}{\lambda_t a}\tanh(\lambda_t(L - a_0)) + \frac{1}{(\lambda_t a)^2}\left(1 - \frac{1}{\cosh(\lambda_t(L - a_0))}\right)\right)^{-1} \times \tilde{U} \tag{B9}$$

Typically, with $\lambda_t(L - a_0) \gg 1$, Eq. (B9) can be simplified to yield Eq. (16). Correspondingly, the tangential displacement at the crack tip ($x = 0$) as given in Eq. (24) can be obtained from either Eq. (B5) or (B6) with Eq. (16). Then, the tangential component of the J-integral in Eq. (22) is obtained as

$$J_2 = \int_0^{\delta_t^*}\sigma_t d\delta_t = \frac{1}{2}K_t\left(\delta_t^*\right)^2 = \frac{9a^2\bar{P}^2}{4\bar{E}b^2h^3}\left(1 + \frac{1}{\lambda_t a}\right)^2 \tag{B10}$$

Furthermore, consider the case with a constant rate of separation $\dot{\Delta}$ at the loading end with a particular displacement ratio, Δ_2/Δ_1. We can solve the governing equations for the DCB specimen with the linear traction-separation relations and proper boundary conditions to determine the other measurable quantities, including $\tilde{P}$, $\bar{P}$, U_1, U_2, Θ_1 and Θ_2, for a given initial crack length (a_0). Then, the corresponding components of the J-integral (J_1 and J_2) and the crack-tip displacements (δ_n^* and δ_t^*) can also be determined. For this purpose, we first write the normal and shear tractions along the interface ($x > 0$) as follows:

$$\sigma_n(x) = K_n\delta_n(x) \tag{B11}$$

$$\sigma_t(x) = K_t\delta_t(x) \tag{B12}$$

where $\delta_t(x)$ is obtained in Eq. (B6) and

$$\delta_n(x) = \left[A_1\cos\left(\lambda_n x'\right) + A_2\sin\left(\lambda_n x'\right)\right]\sinh\left(\lambda_n x'\right) - A_1 \times \sin\left(\lambda_n x'\right)\cosh\left(\lambda_n x'\right) \tag{B13}$$

$$A_1 = \frac{6\tilde{P}}{\bar{E}bh^3\lambda_n^3}\left[\lambda_n a\frac{\sin\left(\lambda_n L'\right)}{\sinh\left(\lambda_n L'\right)} - (\lambda_n a + 1)\frac{\cos\left(\lambda_n L'\right)}{\sinh\left(\lambda_n L'\right)}\right] \tag{B14}$$

$$A_2 = \frac{6\tilde{P}}{\bar{E}bh^3\lambda_n^3}\left[(2\lambda_n a+1)\frac{\cos\left(\lambda_n L'\right)}{\sinh\left(\lambda_n L'\right)}+\frac{\sin\left(\lambda_n L'\right)}{\sinh\left(\lambda_n L'\right)}\right] \tag{B15}$$

with $x' = x-(L-a)$ and $L' = L-a$. Note that the shear traction is proportional to $\bar{P} = P_1 + P_2$, which vanishes for the case of symmetrical loading ($P_2 = -P_1$) as expected for the mode-I condition. Similarly, the normal traction is proportional to $\tilde{P} = P_1 - P_2$, which vanishes for the case of anti-symmetrical loading ($P_2 = P_1$) as expected for the mode-II condition. Both tractions become infinite (singular) at the crack tip ($x = 0$) when $K_t, K_n \to \infty$ as expected from LEFM.

Next, with the normal and shear tractions along the interface, we solve the governing equations for the upper beam only:

$$\bar{E}h\frac{d^2u_{10}}{dx^2} = \sigma_t \tag{B16}$$

$$\frac{\bar{E}h^3}{12}\frac{d^4w_1}{dx^4} = -\sigma_n + \frac{h}{2}\frac{d\sigma_t}{dx} \tag{B17}$$

where w_1 is the normal displacement (deflection) and u_{10} is the axial displacement at the neutral plane of the upper beam.

Since both σ_n and σ_t are zero for the fractured part of the beam ($x < 0$), the governing equations in (B16) and (B17) can be integrated to yield the normal deflection, the tangential displacement, and the rotation at the loading end ($x = -a$) as:

$$\Delta_1 = w_1^* + \theta_1^* a + \frac{4P_1a^3}{\bar{E}bh^3} \tag{B18}$$

$$U_1 = u_{10}^* - \frac{1}{2}\theta_1^* h - \frac{3P_1a^2}{\bar{E}bh^2} \tag{B19}$$

$$\Theta_1 = \theta_1^* + \frac{6P_1a^2}{\bar{E}bh^3} \tag{B20}$$

where w_1^*, θ_1^* and u_{10}^* are to be determined at the crack tip ($x = 0$).

For $x > 0$, the governing equations in (B16) and (B17) are solved with the tractions in Eqs. (B11) and (B12), which leads to

$$u_{10}^* = \frac{3\bar{P}a^2}{4\bar{E}bh^2}\left[-\left(\frac{1}{\lambda_t a}\right)^2(1+\lambda_t a)+\frac{(L-a)^2}{2a^2}+\frac{L-a}{a}\right] \tag{B21}$$

$$\theta_1^* = \frac{3\tilde{P}}{\bar{E}bh^3\lambda_n^2}(2\lambda_n a+1) + \frac{3\bar{P}}{4\bar{E}bh^3\lambda_t^2}\left[\lambda_t^2(L-a)^2+2\lambda_t^2 a(L-a)+6\lambda_t a+6\right] \tag{B22}$$

$$w_1^* = \frac{3\tilde{P}}{\bar{E}bh^3\lambda_n^3}(\lambda_n a+1) + \frac{\bar{P}}{4\bar{E}bh^3\lambda_t^3}\left[\lambda_t^3(L-a)^2(2L+a)+18\lambda_t L-18\right] \tag{B23}$$

Finally, by inserting Eqs. (B21-B23) into Eqs. (B18-B20), we obtain Eqs. (17–19), with which all the measurable quantities, including $\tilde{P}$, $\bar{P}$, U_1, U_2, Θ_1 and Θ_2, can be determined as functions of the applied displacements (Δ_1 and Δ_2) for a given initial crack length ($a = a_0$).

Table C1
List of uncertainties in directly measured quantities.

Direct measurements	Uncertainty	Determined by
Length	0.001 mm	Caliper
Displacement	0.0016 mm	Camera resolution
Force	0.0001 N	Load cell

Appendix C. Uncertainty estimates for crack tip displacement and J-integral components

The uncertainty of the measurements of the normal and shear components of the crack tip displacement are estimated on the basis of the Pythagorean measure of the propagation of error from directly measured quantities. The directly measured quantities are length (calipers), displacement (DIC) and force (load cell). The uncertainties in these measurements are provided in Table C1.

Considering the crack tip opening displacement (Eqn. (11)) as an example, we express it generally as

$$\delta_n^* = f(\Delta, P, \theta, a, D) \tag{C1}$$

Based on the linearized approximation for the propagation of error, the uncertainty of the crack tip opening displacement is estimated as

$$u_{\delta_n^*} = \sqrt{\left(\frac{\partial f}{\partial \Delta}\right)^2 u_\Delta^2 + \left(\frac{\partial f}{\partial P}\right)^2 u_P^2 + \left(\frac{\partial f}{\partial \theta}\right)^2 u_\theta^2 + \left(\frac{\partial f}{\partial a}\right)^2 u_a^2 + \left(\frac{\partial f}{\partial D}\right)^2 u_D^2} \tag{C2}$$

The quantities (θ, a, D) are also indirect and their uncertainty was obtained from direct measurements following the ideas contained in Eqn. (C1-C2). The relative uncertainties (uncertainty of a quantity divided by the absolute value of the quantity itself) were evaluated from the data at each value of the applied displacement Δ_1 because the dependent variables are not all simple power laws of the independent variables. Had that been the case, an analytical form for the relative error could have been developed. The results of this exercise are shown in Fig. C1 for both components of the crack tip displacements at an applied displacement rate $\dot{\Delta}_1$ of 0.625 mm/s. The shear component and the normal component are respectively neglected in the nominally mode I and mode II cases.

A similar exercise was conducted for the components of the J-integral based on Eqns. (9–10) and the results are shown in Fig. C2.

Some observations are made based on the results shown in both figures:

1. The relative error in all cases decreases with increasing applied displacement levels.
2. Most of the data points have relative uncertainties that are well below 2% for the crack tip displacements and 0.1% for J-integrals (dashed lines in each plot). There are a few points in each case where the relative error is higher, but these are for the lowest levels of applied displacements
3. As the mode-mix increases, the uncertainty of the normal component exceeds that of the shear component.
4. The relative error in J-integrals is much smaller than that of the crack tip displacements because the crack length does not appear explicitly in Eqns. (9–10). That said, the assignment of values to J_c does depend on the selection of the crack length for the onset of growth as discussed around Fig. 13b.

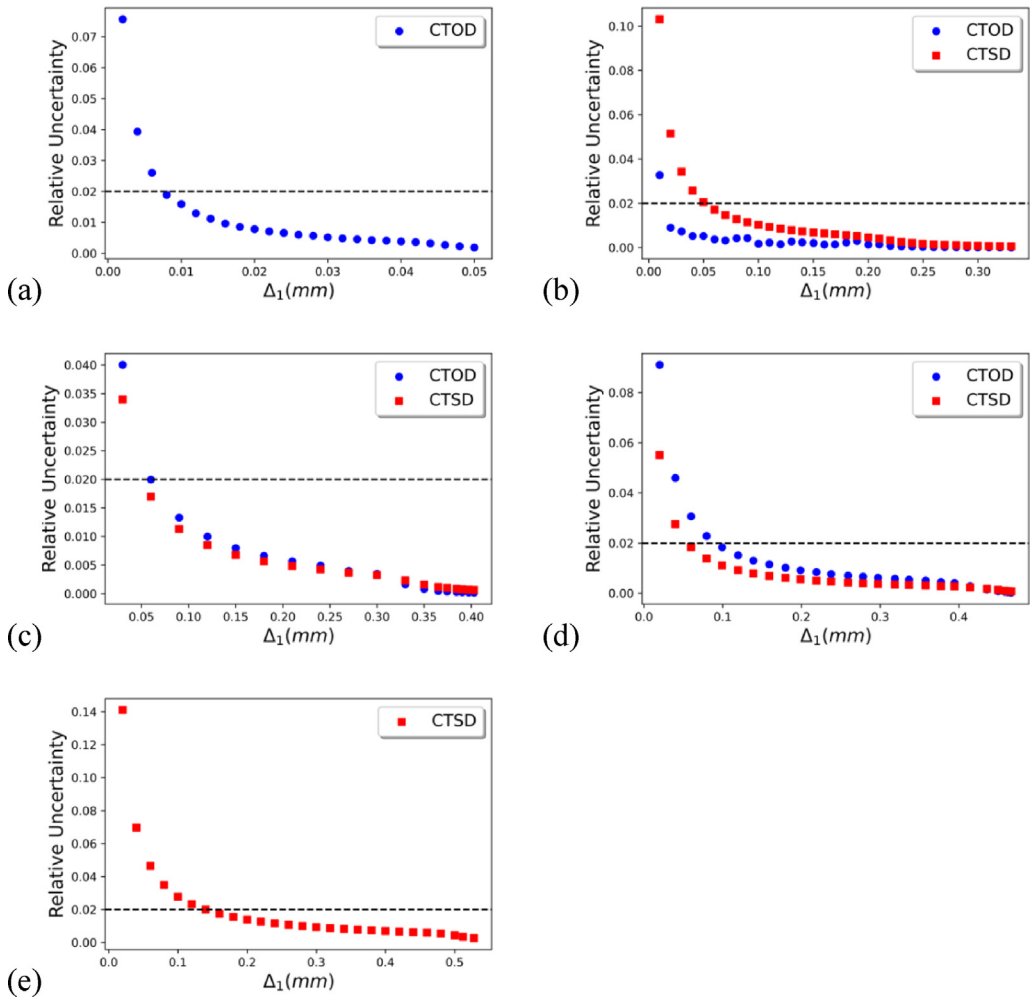

Fig. C1. The relative uncertainty of crack tip opening displacements (CTOD) and crack tip shear displacements (CTSD) at an applied displacement rate $\dot{\Delta}_1$ of 0.625 mm/s at applied displacement ratios (Δ_2/Δ_1) of (a) 0, (b) 0.5, (c) 0.7 and (d) 0.8 and (e) 0.95. The dashed lines indicate a relative error of 2% on each plot.

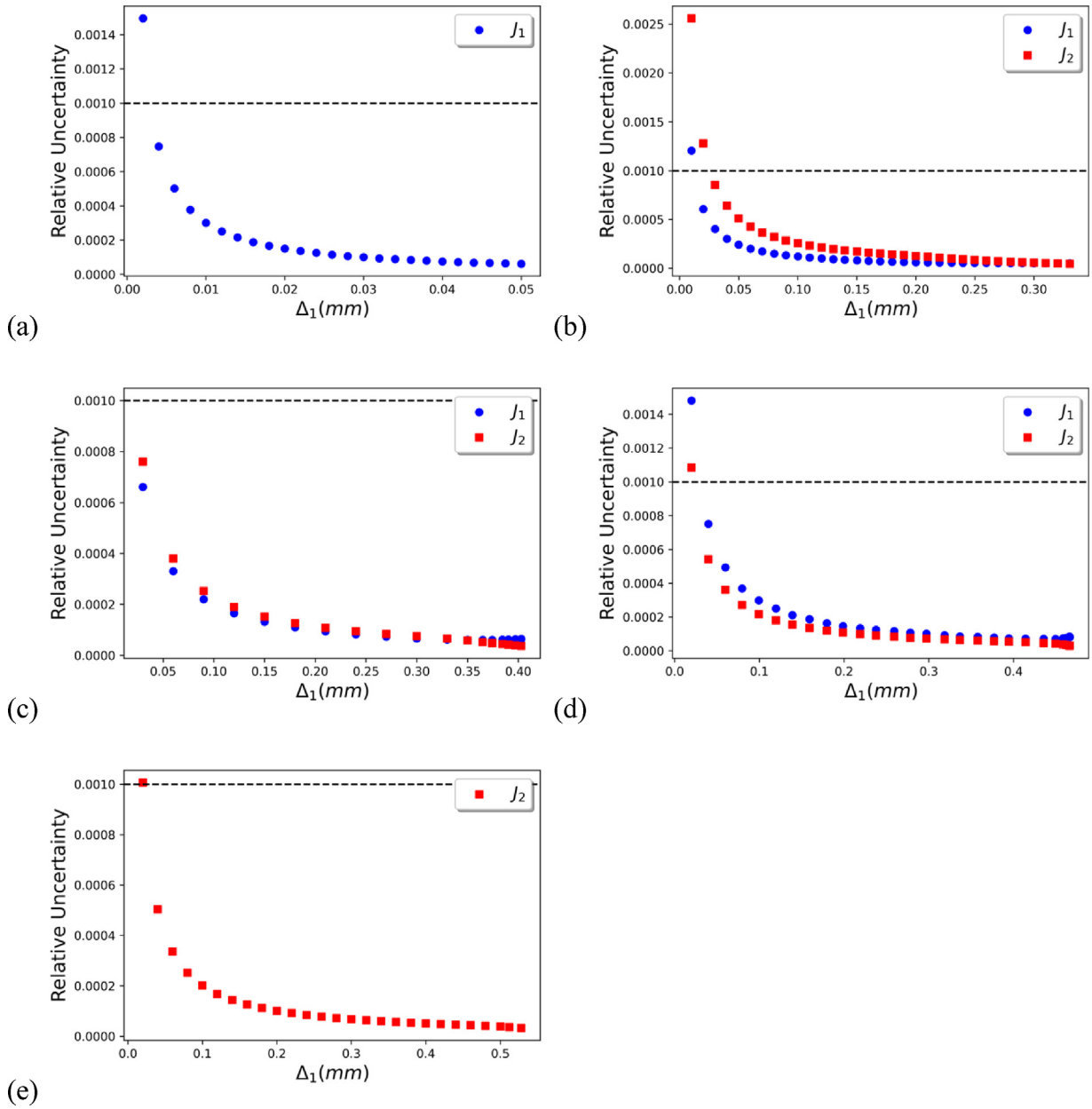

Fig. C2. The relative uncertainty of the J-integral components, at an applied displacement rate $\dot{\Delta}_1$ of 0.625 mm/s at applied displacement ratios (Δ_2/Δ_1) of (a) 0, (b) 0.5, (c) 0.7 and (d) 0.8 and (e) 0.95. The dashed lines indicate a relative error of 0.1% on each plot.

Appendix D. Supplementary data

Supplementary data to this article can be found online at https://doi.org/10.1016/j.ijsolstr.2021.111129.

References

Barenblatt, G.I., 1959. The formation of equilibrium cracks during brittle fracture. General ideas and hypotheses. Axially-symmetric cracks. J. Appl. Math. Mech. 23 (3), 622–636.

Blackman, B., Hadavinia, H., Kinloch, A.J., Williams, J., 2003. The use of a cohesive zone model to study the fracture of fibre composites and adhesively-bonded joints. Int. J. Fracture 119, 25–46.

Blaysat, B., Hoefnagels, J.P.M., Lubineau, G., Alfano, M., Geers, M.G.D., 2015. Interface debonding characterization by image correlation integrated with double cantilever beam kinematics. Int. J. Solids and Structures 55, 79–91.

Brussat, T., Chiu, S., Mostovoy, S., 1977. Fracture mechanics for structural adhesive bonds. LOCKHEED-CALIFORNIA CO BURBANK.

Cao, H.C., Evans, A.G., 1989. An experimental study of the fracture resistance of bimaterial interfaces. Mech. Mater. 7 (4), 295–304.

Chai, Y.S., Liechti, K.M., 1991. Biaxial loading experiments for determining interfacial fracture toughness. J. Appl. Mech. 58, 680–687.

Chai, Y.S., Liechti, K.M., 1992. Asymmetric shielding in interfacial fracture under in-plane shear. J. Appl. Mech. 59, 295–304.

Charalambides, P.G., Cao, H.C., Lund, J., Evans, A.G., 1990. Development of a test method for measuring the mixed mode fracture resistance of bimaterial interfaces. Mech. Mater. 8 (4), 269–283.

Chow, C.L., Woo, C.W., Sykes, J.L., 1979. On the determination and application of COD to epoxy-bonded aluminum joints. J. Strain Anal. Eng. Des. 14, 37–42.

Conroy, M., Kinloch, A.J., Williams, J.G., Ivankovic, A., 2015. Mixed mode partitioning of beam-like geometries: A damage dependent solution. Eng. Fract. Mech. 149, 351–367.

Davidson, B.D., Sediles, F.O., 2011. Mixed-mode I-II–III delamination toughness determination via a shear–torsion-bending test. Compos. A Appl. Sci. Manuf. 42 (6), 589–603.

Dillard, D.A., Mukherjee, B., Karnal, P., Batra, R.C., Frechette, J., 2018. A review of Winkler's foundation and its profound influence on adhesion and soft matter applications. Soft Matter 14 (19), 3669–3683.

Dugdale, D.S., 1960. Yielding of steel sheets containing slits. J. Mech. Phys. Solids 8 (2), 100–104.

Evans, A.G., Rühle, M., Dalgleish, B.J., Charalambides, P.G., 1990. The fracture energy of bimaterial interfaces. Metall. Trans. A 21 (9), 2419–2429.

Evans, A.G., Hutchinson, J.W., 1989. Effects of non-planarity on the mixed mode fracture resistance of bimaterial interfaces. Acta Metall. 37 (3), 909–916.
Fernlund, G., Spelt, J.K., 1994. Mixed-mode fracture characterization of adhesive joints. Compos. Sci. Technol. 50 (4), 441–449.
Gorman, J.M., Thouless, M.D., 2019. The use of digital-image correlation to investigate the cohesive zone in a double-cantilever beam, with comparisons to numerical and analytical models. J. Mech. Phys. Solids 123, 315–331.
Gowrishankar, S., Mei, H., Liechti, K.M., Huang, R., 2012. A comparison of direct and iterative methods for determining traction-separation relations. Int. J. Fract. 177 (2), 109–128.
Högberg, J.L., Sørensen, B.F., Stigh, U., 2007. Constitutive behaviour of mixed mode loaded adhesive layer. Int. J. Solids and Structures 44 (25-26), 8335–8354.
Hung, S.C., Liechti, K.M., 1997. An evaluation of the Arcan specimen for determining the shear moduli of fiber-reinforced composites. Exp. Mech. 37 (4), 460–468.
Hutchinson, J.W., Suo, Z., 1992. Mixed mode cracking in layered materials. Adv. Appl. Mech. 29, 63–199.
Jacobsen, T.K., Sørensen, B.F., 2001. Mode I intra-laminar crack growth in composites—modelling of R-curves from measured bridging laws. Compos. A Appl. Sci. Manuf. 32 (1), 1–11.
Jain, L.K., Dransfield, K.A., Mai, Y.-W., 1998. Effect of reinforcing tabs on the mode I delamination toughness of stitched CFRPs. J. Compos. Mater. 32 (22), 2016–2041.
Johnson, K.L., Kendall, K., and Roberts, A. D., 1971. Surface energy and the contact of elastic solids. Proceedings of the Royal Society of London. Series A, Mathematical and Physical Sciences 324, 301-313.
Kanninen, M.F., 1973. An augmented double cantilever beam model for studying crack propagation and arrest. Int. J. Fracture 9, 83–92.
Li, S., Thouless, M.D., Waas, A.M., Schroeder, J.A., Zavattieri, P.D., 2006. Mixed-mode cohesive-zone models for fracture of an adhesively bonded polymer matrix composite. Eng. Fracture Mech. 73 (1), 64–78.
Liang, Y.-M., Liechti, K.M., 1995. Toughening mechanisms in mixed-mode interfacial fracture. Int. J. Solids and Structures 32 (6-7), 957–978.
Liechti, K.M., Knauss, W.G., 1982. Crack propagation at material interfaces: I. Experimental technique to determine crack profiles. Exp. Mech. 22 (7), 262–269.
Lindhagen, J.E., Berglund, L.A., 2000. Application of bridging-law concepts to short-fibre compositesPart 1: DCB test procedures for bridging law and fracture energy. Compos. Sci. Technol. 60 (6), 871–883.
Mahajan, R.V., Ravi-Chandar, K., 1989. An experimental investigation of mixed-mode fracture. Int. J. Fract. 41 (4), 235–252.
Marzi, S., Rauh, A., Hinterhölzl, R.M., 2014. Fracture mechanical investigations and cohesive zone failure modelling on automotive composites. Compos. Struct. 111, 324–331.
Maugis, D., 1992. Adhesion of spheres: The JKR-DMT transition using a Dugdale model. J. Colloid Interface Sci. 150 (1), 243–269.
Mello, A.V., Liechti, K.M., 2006. The effect of self-assembled monolayers on interfacial fracture. J. Appl. Mech. 73, 860–870.
Mello, A.W., Liechti, K.M., 2004. A piezoelectric biaxial loading device for interfacial fracture experiments. Exp. Mech. 44 (5), 495–501.
Mohammed, I., Liechti, K.M., 2000. Cohesive zone modeling of crack nucleation at bimaterial corners. J. Mech. Phys. Solids 48 (4), 735–764.
Needleman, A., 1990. An analysis of tensile decohesion along an interface. J. Mech. Phys. Solids 38 (3), 289–324.
Ouyang, Z., Li, G., 2009. Nonlinear interface shear fracture of end notched flexure specimens. Int. J. Solids Struct. 46 (13), 2659–2668.
Pappas, G.A., Botsis, J., 2020. Variations on R-curves and traction-separation relations in DCB specimens loaded under end opening forces or pure moments. Int. J. Solids and Structures 191, 42–55.
Parmigiani, J.P., Thouless, M.D., 2007. The effects of cohesive strength and toughness on mixed-mode delamination of beam-like geometries. Eng. Fracture Mech. 74 (17), 2675–2699.
Rajan, S., Sutton, M.A., Fuerte, R., Kidane, A., 2018. Traction-separation relationship for polymer-modified bitumen under Mode I loading: Double cantilever beam experiment with stereo digital image correlation. Eng. Fracture Mech. 187, 404–421.
Rajan, S., Sutton, M.A., McMakin, W., Compton, E., Kidane, A., Gurdal, Z., Wehbe, R., Farzana, Y., 2020. Characterization of Mode I and Mode II traction–separation laws for cohesive separation of uncured thermoset tows. Int. J. Fracture 221 (1), 25–38.
Reeder, J.R., Crews, J.H., 1990. Mixed-mode bending method for delamination testing. AIAA J. 28 (7), 1270–1276.
Rice, J.R., 1988. Elastic fracture mechanics concepts for interfacial cracks. J. Appl. Mech. 55, 98–103.
Shirani, A., Liechti, K.M., 1998. A calibrated fracture process zone model for thin film blistering. Int. J. Fracture 93, 281–314.
Sills, R.B., Thouless, M.D., 2013. The effect of cohesive-law parameters on mixed-mode fracture. Eng. Fracture Mech. 109, 353–368.
Singh, H.K., Chakraborty, A., Frazier, C.E., Dillard, D.A., 2010. Mixed mode fracture testing of adhesively bonded wood specimens using a dual actuator load frame. Holzforschung 64, 353–361.
Sørensen, B., Jacobsen, T., 2009. Delamination of fibre composites: determination of mixed mode cohesive laws. Compos Sci Tech 69, 445–456.
Sorensen, B.F., 2002. Cohesive law and notch sensitivity of adhesive joints. Acta Mater. 50 (5), 1053–1061.
Sorensen, B.F., Jacobsen, T.K., 2003. Determination of cohesive laws by the J integral approach. Eng. Fracture Mech. 70 (14), 1841–1858.
Sørensen, B.F., Jacobsen, T.K., 1998. Large-scale bridging in composites: R-curves and bridging laws. Compos. A Appl. Sci. Manuf. 29, 1443–1451.
Sundararaman, V., Davidson, B.D., 1997. An unsymmetric double cantilever beam test for interfacial fracture toughness determination. Int. J. Solids and Structures 34 (7), 799–817.
Suo, Z., Bao, G., Fan, B., 1992. Delamination R-curve phenomena due to damage. J. Mech. Phys. Solids 40 (1), 1–16.
Swadener, J.G., Liechti, K.M., 1998. Asymmetric shielding mechanisms in the mixed-mode fracture of a glass/epoxy interface. J. Appl. Mech. 65, 25–29.
Ungsuwarungsri, T., Knauss, W.G., 1987. The role of damage-softened material behavior in the fracture of composites and adhesives. Int. J. Fracture 35 (3), 221–241.
Vanlandingham, M.R., Eduljee, R.F., Gillespie Jr., J.W., 1999. Relationships between stoichiometry, microstructure, and properties for amine-cured epoxies. J. Appl. Polym. Sci. 71 (5), 699–712.
Wang, H., Vu-Khanh, T., 1996. Use of end-loaded-split (ELS) test to study stable fracture behaviour of composites under mode II loading. Compos. Struct. 36 (1-2), 71–79.
Wang, J.-S., Suo, Z., 1990. Experimental-determination of interfacial toughness curves using Brazil-nut-sandwiches. Acta Metall. Mater. 38 (7), 1279–1290.
Williams, J.G., 1989. End corrections for orthotropic DCB specimens. Compos. Sci. Technol. 35 (4), 367–376.
Williams, M., 1959. The stresses around a fault or crack in dissimilar media. Bulletin of the Seismological Society of America 49, 199-204.
Wu, C., Gowrishankar, S., Huang, R., Liechti, K.M., 2016. On determining mixed-mode traction–separation relations for interfaces. Int. J. Fract. 202 (1), 1–19.
Wu, C., Huang, R., Liechti, K.M., 2019. Simultaneous extraction of tensile and shear interactions at interfaces. J. Mech. Phys. Solids 125, 225–254.
Xiao, F., Hui, C.-Y., Kramer, E.J., 1993. Analysis of a mixed mode fracture specimen: the asymmetric double cantilever beam. J. Mater. Sci. 28 (20), 5620–5629.
Yang, T., Liechti, K.M., Huang, R., 2020. A multiscale cohesive zone model for rate-dependent fracture of interfaces. J. Mech. Phys. Solids 145, 104142. https://doi.org/10.1016/j.jmps.2020.104142.
Yang, T., Yang, X., Huang, R., Liechti, K.M., 2019. Rate-dependent traction-separation relations for a silicon/epoxy interface Informed by experiments and bond rupture kinetics. J. Mech. Phys. Solids 131, 1–19.